High shear strain behaviour of synthetic muscovite fault gouges under hydrothermal conditions

Esther W.E. Van Diggelen*, Johannes H.P. De Bresser, Colin J. Peach, Christopher J. Spiers

Faculty of Geosciences, Utrecht University, P.O. Box 80.021, 3508 TA Utrecht, Netherlands

ABSTRACT

Major continental fault zones typically contain phyllosilicates and have long been recognised as zones of persistent weakness. To establish whether the presence of micas can explain this weakness, we studied the frictional behaviour of simulated muscovite fault gouge by performing rotary shear experiments in the temperature range 20–700 °C, under constant effective normal stresses of 20–100 MPa, a fixed fluid pressure of 100 MPa and at sliding velocities of 0.03–3.7 μm/s, reaching shear strains up to 100. Cataclasis causes substantial grain size reduction up to 600 °C. With increasing strain, both pervasive and localized cataclasis and related compaction result in strain hardening, until steady state is reached. This reflects the progressive development of a continuous network of fine grained, hardening bands. Coarse grained relict lenses between these bands show folded and kinked muscovite grains indicative of ductile mechanisms. Samples deformed at 700 °C show evidence for chemical alteration and partial melting. Since our data suggest that muscovite gouge strengthens with depth and strain, it is questionable whether its presence can contribute to the long-term weakness of major crustal fault zones, unless a substantial decrease in strength occurs at shear strain rates lower than attained in our study.

© 2009 Elsevier Ltd. All rights reserved.

1. Introduction

Major continental fault zones have long been recognised by field geologists as zones of highly localized deformation and hence of persistent weakness (Balfour et al., 2005; Holdsworth et al., 2001; Imber et al., 1997; Jefferies et al., 2006b; Rutter et al., 2001; White et al., 1986; Zoback et al., 2007; Zoback et al., 1987). The implication is that the quartz-, feldspar-, and phyllosilicate-rich fault rocks often found within such faults must be weaker than the surrounding country rock. Laboratory rock friction experiments have confirmed that typical continental fault rocks are indeed weak compared to intact quartzo-feldspathic host rocks (Bos et al., 2000; Dieterich, 1978; Hickman, 1991; Holdsworth, 2004; Lachenbruch and Sass, 1980; Logan and Rauenzahn, 1987; Morrow et al., 2000; Morrow et al., 1992; Niemeijer and Spiers, 2005, 2006; Shimamoto and Logan, 1981; Takahashi et al., 2007).

Lab data for long-term fault strength are usually expressed in terms of Byerlee's Rule for fault friction (friction coefficient $\mu = 0.6$–0.9) giving way to plastic flow at depths of 10–15 km, thus producing the classical "Christmas Tree" strength profile (Bos and Spiers, 2002; Byerlee, 1978; Goetze and Evans, 1979; Holdsworth

et al., 2001; Niemeijer and Spiers, 2005). Such profiles fit well with the depth distribution of seismicity on major faults (Scholz, 2002; Sibson, 1983). However, laboratory-based strength profiles are not fully consistent with other geophysical observations on major mature fault zones, like the San Andreas fault zone. In the case of the San Andreas fault, the lack of a positive heat flow anomaly, and the high angles ($\sim 70°$) measured between the in-situ principal stress σ_1 and the fault surface (Townend and Zoback, 2004; Zoback et al., 2007), imply a low mean resolved shear stress on the fault of around 10–20 MPa (Lachenbruch and Sass, 1980; Zoback et al., 1987) and a coefficient of friction of only ~ 0.2. This is far less than measured for (simulated) fault rocks in laboratory experiments (Blanpied et al., 1995; Bos and Spiers, 2000; Byerlee, 1978; Carpenter et al., 2009; Moore and Lockner, 2004; Morrow et al., 2000; Morrow et al., 1992; Nakatani and Scholz, 2004; Niemeijer and Spiers, 2005; Tembe et al., 2006a; Tembe et al., 2006b).

A widely proposed explanation for the inferred long-term weakness of major crustal faults is that high pore fluid pressure reduces the effective shear stress required for slip. Fluids released during compaction and/or dehydration reactions at depth might locally increase fluid pressures to approach lithostatic values (Byerlee, 1990; Collettini and Barchi, 2002; Faulkner and Rutter, 2001; Hickman et al., 1995; Miller et al., 1996; Miller and Olgaard, 1997; Sibson, 2004; Sleep, 1995). However, fluid pressures inside a fault can only increase if the zone has a low permeability, caused

* Corresponding author. Tel.: +31 30 2535079; fax: +31 30 2537725.
E-mail address: diggelen@geo.uu.nl (E.W.E. Van Diggelen).

by ubiquitous phyllosilicates or continuous wall rock cementation (Schleicher et al., 2008; Schleicher et al., 2009b; Zhang et al., 2001). Faulkner and Rutter (2001) showed that dehydration of phyllosilicates (assuming 50% phyllosilicate content at 15–20 km depth) is sufficient to maintain an elevated fluid pressure for ~12 ky, but insufficient to weaken a large fault on geologic timescales. Moreover, in-situ measurements in fault zones show little evidence for continuously high fluid pressures (Wintsch et al., 1995). In particular, fluid pressure measurements in the SAFOD (San Andreas Fault Observatory at Depth) drill hole indicate near-hydrostatic rather than lithostatic fluid pressures at depths up to 3.5 km (Tembe et al., 2006b; Zoback et al., 2007). It thus seems unlikely that high fluid pressures alone can account for the apparent long-term weakness of large scale fault zones.

Alternatively, the presence of relatively weak reaction product minerals, such as clays, micas, chlorite or talc may explain the inferred weakness of major faults (Arancibia and Morata, 2005; Jefferies et al., 2006a; Logan and Rauenzahn, 1987; O'Hara, 2007; Shea and Kronenberg, 1992; Wibberley, 1999; Wintsch et al., 1995). Experiments have shown that many such phyllosilicates are significantly weaker than quartz and feldspars (Ikari et al., 2007; Logan and Rauenzahn, 1987; Mariani et al., 2006; Moore and Lockner, 2004; Moore and Lockner, 2007; Moore et al., 1997; Morrow et al., 2000; Morrow et al., 1992; Shimamoto and Logan, 1981) and are stable up to 15 km depth. It follows that a continuous, through-going foliation of phyllosilicate minerals may strongly influence fault zone rheology on a crustal scale (Holdsworth et al., 2001; Imber et al., 1997; Ranalli, 1995; Rutter et al., 2001; Rutter et al., 1986). Reaction-softening of this type has frequently been proposed as an explanation for the weakness of the San Andreas fault zone (Evans and Chester, 1995; Moore and Rymer, 2007; Wintsch et al., 1995). Recently, core material retrieved during SAFOD phase 3 drilling has shown that the actively deforming strands of the fault contain a grayish-black, foliated, phyllosilicate-rich fault gouge. Visible clasts make up about 5% of the rock volume and consist of fragments of serpentinite, sandstone and siltstone protolith (SAFOD core atlas, 2007). These observations confirm that phyllosilicate foliation development and reaction weakening are key processes in determining fault zone rheology.

Additionally, fluid-assisted deformation processes, such as pressure solution, have been put forward as a mechanism for weakening of fault rocks (Blanpied et al., 1995; Chester, 1995; Collettini and Holdsworth, 2004; Hickman et al., 1995; Jefferies et al., 2006b; Kanagawa, 2002; Kanagawa et al., 2000; Lehner and Bataille, 1984; Schleicher et al., 2009a; Wu et al., 1975). Experiments on wet quartz gouge under hydrothermal conditions (Kanagawa et al., 2000; Niemeijer et al., 2002), and on wet granular halite used as an analogue (Bos et al., 2000), show competition between pressure solution, compaction and cataclasis, leading to high frictional strength ($\mu = 0.8$–0.9) at low slip rates. However, experiments on simulated gouges consisting of halite plus kaolinite, or of halite plus muscovite, show a reduction in μ-values to 0.3–0.4 (Bos and Spiers, 2000, 2001; Niemeijer and Spiers, 2005). This is due to the development of a through-going phyllosilicate foliation on which frictional slip occurs with accommodation by pressure solution of the intervening halite clasts. Bos and Spiers (2002) and Niemeijer and Spiers (2005, 2007) developed a microphysical model explaining their experimental results and predicting upper crustal strength–depth profiles for foliated quartz-mica fault rock some 2–5 times weaker than obtained using Byerlee's Rule. The low strength predicted is due to the serial effect of easy pressure solution of quartz clasts at low sliding rates and the low frictional strength ($\mu = 0.3$) assumed for the enveloping phyllosilicate foliation. In the experimental study of Mariani et al. (2006),

pure muscovite fault gouge shows strain rate insensitive strain hardening behaviour at shear strain rates faster than 1.4×10^{-5} s^{-1} at 700 °C and at all strain rates tested (10^{-7} to 10^{-3} s^{-1}) at temperatures of 400–600 °C. This behaviour is primarily attributed to mutual misalignment of mica flakes with contributions from progressive porosity reduction and formation of oblique shear features (Mariani et al., 2006). At 700 °C and strain rates lower than 1.4×10^{-5} s^{-1}, the shear strength drops dramatically. Deformation of the muscovite gouge under these conditions has linear viscous characteristics, possibly due to viscous glide of basal dislocations in the mica becoming rate controlling (Mariani et al., 2006). The above studies imply that both pressure solution and phyllosilicate foliation development may play an important role in weakening major fault zones, and demonstrate a crucial need for laboratory data on the frictional and plastic flow strength of phyllosilicates under conditions close to those in observed in nature.

As discussed, laboratory studies have shown that most phyllosilicate gouges are characterized by significantly lower frictional strength ($\mu = 0.2$–0.5) than Byerlee's Rule predicts (Ikari et al., 2007; Mariani et al., 2006; Moore and Lockner, 2004; Morrow et al., 1992; Niemeijer and Spiers, 2005; Scruggs and Tullis, 1998), especially in the presence of water (Moore and Lockner, 2004; Moore et al., 1997; Morrow et al., 2000). Most laboratory experiments on phyllosilicates have been performed at room temperature and/or at low shear strains ($\gamma < 15$), without a pore fluid. By contrast, upper and mid-crustal fault rocks typically experienced large shear strains at elevated temperatures (50–350 °C) in the presence of a chemically active pore fluid. In order to improve our understanding of fault zone deformation processes and the role of phyllosilicates under upper and mid-crustal conditions, it is, therefore, necessary to perform rock friction experiments on realistic gouge compositions under hydrothermal conditions, and towards shear strains that better correspond with natural settings. High temperatures (300–700 °C) and elevated fluid pressures (up to 103 MPa) were attained by Mariani et al. (2006) in their experimental study of muscovite fault gouge, but the saw-cut deformation geometry they applied did not allow high shear strains to be reached (γ for most experiments in the order of 2.3), and constant normal stress was difficult to maintain (He et al., 2007, 2006). In contrast, large shear strains under controlled normal stress were reached in various types of gouges by Scruggs and Tullis (1998) using an experimental rotary shear set-up, but no experiments other than at room temperature were performed.

The present study focuses on determining the frictional behaviour of simulated muscovite fault gouge at shear strains above 20 and occasionally even up to 100, under hydrothermal conditions in the temperature range 20–700 °C. In our tests we applied constant, controlled effective normal stresses of 20–100 MPa, at a fixed fluid pressure of 100 MPa with deionised water as the pore fluid. Samples were typically deformed at sliding velocities in the range 0.03–3.7 μm/s, corresponding to shear strain rates of ~10^{-5} to 10^{-3} s^{-1}. We chose to investigate muscovite because it is a principal phyllosilicate constituent of many exhumed upper and mid-crustal faults, and because relatively little data exists to support the μ-value of 0.3 for muscovite used in recent models for fault strength (Bos and Spiers, 2002; Niemeijer and Spiers, 2005; Niemeijer and Spiers, 2007). The effects of normal stress, sliding velocity, displacement (i.e. shear strain) and temperature on the frictional behaviour of the muscovite gouges were determined and combined with the results of microstructural analysis of the deformed samples to elucidate the operative microphysical processes. The mechanical data obtained are used to construct a strength profile for a muscovite-dominated fault, assuming a thermal gradient and other conditions similar to those pertaining to the San Andreas fault zone.

2. Experimental approach

Our experiments consisted of high strain rotary shear experiments performed on fine grained granular muscovite samples (simulated muscovite fault gouge) under hydrothermal conditions ($P_f = 100$ MPa, $T = 20$–700 °C). We primarily aimed to determine friction coefficient and microstructural development as a function of shear strain (γ up to 100), effective normal stress ($\sigma_{eff} = 20$–100 MPa), temperature ($T = 20$–700 °C), and sliding velocity ($V = 0.03$–3.7 µm/s).

2.1. Starting material

The synthetic fault gouge material used in this study is a natural muscovite powder (Mica S), commercially obtained from Internatio B.V. and originally mined in Aspang, Austria. The chemical composition of the muscovite is $K_{1.97}Na_{0.07}$ ($Al_{3.02}Fe_{0.94}Mg_{0.50}$) ($Si_{7.27}Al_{1.51}$) O_{20} $(OH)_4$, determined using a Jeol JXA-8600 superprobe microprobe and assuming four formula units for the hydroxyl group and normalized to oxygen. This material was previously used in the experiments reported by Niemeijer and Spiers (2005, 2006). Particle size analysis, performed using a Malvern particle sizer, showed that the median grain size of the muscovite was ~13 µm (equivalent spherical diameter), with 90% of the grains lying between 3 and 50 µm in size. Microprobe and Energy Dispersive X-ray (EDX) analysis showed that the bulk material also contained quartz (<10 vol%), apatite (<0.1 vol%), zircon (<0.1 vol%), and calcium-carbonate (<0.1 vol%).

2.2. Experimental apparatus

The hydrothermal rotary shear apparatus, described in detail by Niemeijer et al. (2008), was used to perform our high shear strain experiments on the synthetic muscovite fault gouges (Fig. 1). In this machine, the synthetic fault gouge sample is located between a pair of opposing internal pistons made of René 41 with a mullite core to reduce axial heat loss. The initially ~1 mm thick gouge sample is kept in place by a set of two mildly hardened stainless steel confining rings (Thyssen type 1.4122), with an inner radius of 14 and 11 mm, respectively (Fig. 1c and d). To prevent localization of slip along the piston–sample interface, a cross-hatch pattern has been machined on the piston surfaces in contact with the sample. This pattern consists of two sets of grooves 0.5 mm apart and roughly 0.2 mm depth, resulting in asperities with a surface area of ~0.25 mm², and has been roughened further by dry-sandblasting with glass beads (diameter 120 µm) for extra grip on the gouge.

During a test, the piston-sample assembly is positioned inside a 300 MPa pressure vessel, which in turn is located in an Instron 1362 loading frame (Fig. 1a). The top of the piston-sample assembly is coupled to a pressure-compensated piston in the upper sealing head. This piston in turn locks into the upper forcing block and the attached torque and axial force gauge couple. Axial force is applied to the forcing block via a low friction bearing and measured using an in-line Instron load cell. The lower piston fits into a rotation-proof slot in the bottom of the pressure vessel, which is itself rigidly mounted in the lower forcing block (Fig. 1a). This is coupled to the underlying servo-controlled, rotational drive system, which in turn is rigidly coupled to the vertical Instron loading ram.

Normal stress is applied using the Instron loading ram, and is measured externally by means of the (100 kN) Instron load cell that can be held constant to within 0.2 MPa. Pore fluid pressure is applied directly to the sample by pressurizing the sealed vessel with deionised water using a manually driven high pressure pump. The fluid pressure is measured externally using a pressure transducer with a resolution of 0.005 MPa. The sample is heated using an internally mounted 3 kW Inconel-sheathed furnace element (Fig. 1b). Temperatures up to 700 °C are continuously measured to within 1 °C using two K-type thermocouples, one located in the furnace element and the other mounted ~5 mm below the sample at a similar distance from the furnace element as the gouge. The main vessel seals (upper + lower O-rings and outer skin) are cooled by means of a water cooling system at a flow rate of typically 3 l/min. Vertical displacement of the upper (pressure-compensated) loading piston, and hence compaction/dilatation normal to the synthetic fault gouge, is externally measured using a linear variable differential transformer (LVDT) located in the Instron loading ram assembly, with a resolution of 0.005 mm.

The servo-controlled motor and gearbox system, located on the Instron ram, rotates the vessel and the internally fixed lower piston at a fixed rate, producing sliding velocities within the sample of 0.03–3.7 µm/s (equivalent to shear strain rates of the order of 10^{-5} to 10^{-3} s^{-1}), while the upper piston and coupled pressure-compensated piston remain stationary with respect to the Instron loading frame. Shear displacements up to ~80 mm (equivalent to a shear strain γ of up to 130) are measured using an external potentiometer with an accuracy of 0.001 mm, connected to the lower (rotating) forcing block. Shear stress is measured externally with an equivalent accuracy of 0.2 MPa (zero machine-friction case), using the torque gauge couple mounted on the upper forcing block. The measured shear stress reflects the total mechanical resistance to rotation and thus needs to be corrected for apparatus friction, i.e., the frictional force exerted by the seals and by the confining rings surrounding the gouge.

2.3. Experimental procedure

In each experiment, 0.30 g of sample material was loaded onto one of the piston surfaces with the confining rings in place. The material was then uniformly distributed over the piston surface and lightly pre-compacted creating a layer ~1 mm in thickness, after which the opposing piston was lowered into the confining rings and fixed with the retaining screw (Fig. 1d). The piston-sample assembly was subsequently lowered into the water–primed vessel, which in turn was sealed and placed in the Instron 1362 loading frame. The vessel was then moved upwards using the Instron ram, and the piston assembly was engaged with the upper forcing block plus the torque and axial force gauges.

After heating to the desired test temperature (<30 min) and applying a fluid pressure of 100 MPa, a normal stress up to 200 MPa was applied using the Instron. The system was then left to equilibrate thermally for 45 min. During this time, the sample compacted from about 40% to 25–30% porosity (see Section 2.4), i.e., to a thickness of ~0.6 mm. After equilibration, the rotary drive was typically switched on to give a sliding velocity of 1.0 µm/s until a displacement of ~10 mm was reached, beyond which the effective normal stress or sliding velocity were systematically varied.

The following types of experiments were performed at a fixed fluid pressure of 100 MPa:

(1) sliding experiments at constant effective normal stress ($\sigma_{eff} = 100$ MPa) and temperature ($T = 500$ °C), and at fixed sliding velocities of $V = 0.1$, 1.0 and 3.7 µm/s;
(2) experiments at constant effective normal stress ($\sigma_{eff} = 100$ MPa) and sliding velocity ($V = 1.0$ µm/s), and at a constant temperature of 100, 300, 500 and 700 °C;
(3) normal stress-stepping experiments ($\sigma_{eff} = 20$, 40, 60, 80 and 100 MPa) at constant sliding velocity ($V = 1.0$ µm/s) and at fixed temperature ($T = 20$, 150, 225, 300, 400, 500, 600 and 700 °C); and
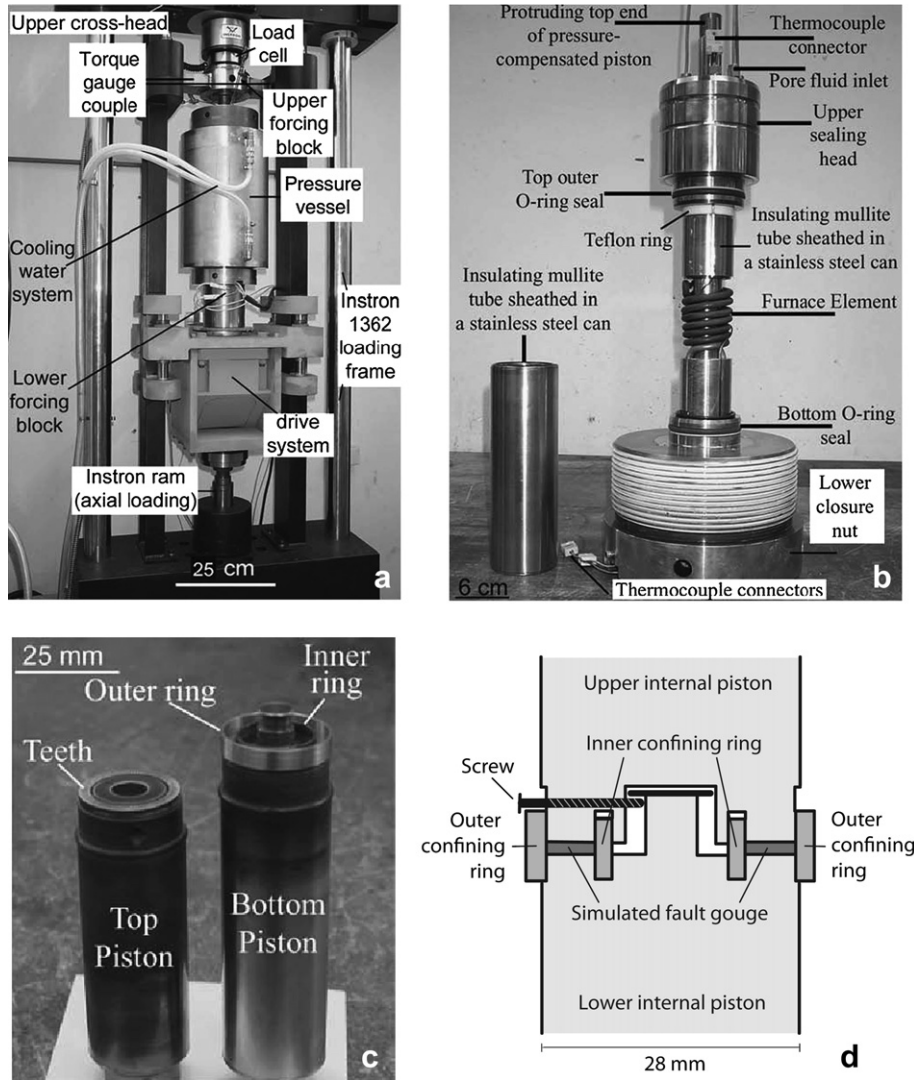
Fig. 1. Hydrothermal rotary shear apparatus used in the present study. (a) The rotary shear drive system and pressure vessel mounted inside the Instron loading frame. (b) The two internal pistons assembled with the pressure-compensated upper sealing head. The insulating mullite tubes sheathed with stainless steel and the furnace element are normally located inside the vessel prior to assembly. (c) The two internal pistons with sample confining rings. The internal pistons are made of René 41 and have a core of mullite to reduce heat loss along the pistons. The confining rings were made of mild hardened stainless steel type 1.4122, suitable for use even at temperatures up to 700 °C. (d) Schematic cross section of the piston assembly showing the position of the fault gouge sample.

(4) velocity-stepping experiments ($V = 0.03, 0.1, 0.5, 1, 3.7$ µm/s) at constant effective normal stress ($\sigma_{eff} = 100$ MPa) and at fixed temperature ($T = 20, 150, 225, 300, 400, 500, 600,$ and 700 °C).

For control purposes, one additional compaction experiment (no shear displacement) was performed at $T = 700$ °C and $\sigma_{eff} = 100$ MPa. The main purpose of this experiment was to seek evidence for any chemical breakdown or partial melting of muscovite, or for possible healing mechanisms that might otherwise be destroyed during shear. To maximize the chance of detecting such effects, the duration of the experiment was 166 h (about 1 week), which is 5–20 times longer than the other experiments performed.

Note that the normal stress-stepping experiments performed at $V = 1.0$ µm/s (type 3 above) were carried out to determine the coefficient of friction of the samples at different temperatures. Prior to the first step in stress, the samples were sheared at an effective normal stress of 20 MPa until a shear strain of 13–16 (displacement of 8–10 mm) was reached with respect to the initial gouge thickness of 0.62 mm. The effective normal stress was then stepped up, with a step size of 20 MPa, to 100 MPa and back down to 20 MPa (Niemeijer and Spiers, 2007; Niemeijer et al., 2008). A shear strain of ∼1.6 (displacement of 1 mm) was typically sufficient to reach steady state shear stress levels in an individual stress step. In the velocity-stepping experiments (type 4 above), the gouges were sheared prior to the stepping sequence at an effective normal stress of 100 MPa and at a constant sliding velocity of 1.0 µm/s. After a shear strain of ∼16 (displacement of 10 mm) was reached, the velocity was typically stepped to 3.7, 0.1, 1.0, 0.03, 1.0 and 0.5 µm/s, respectively. In most steps, a shear strain of ∼1.6 (displacement of 1 mm) was again sufficient to reach steady state shear stress levels.

After each shear experiment, the rotary drive and furnace were turned off, resulting in an immediate decrease in temperature and pore fluid pressure. The system cooled to room temperature within 20 min, after which the axial load was removed and the water cooling was switched off. The pistons and sample material were then taken out and left to dry in an oven at 60 °C for at least 45 min. All experiments and corresponding conditions are listed in Table 1.

Table 1

Sliding experiments at constant conditions (non-stepping), $\sigma_{eff} = 100$ MPa

Experiment	Temperature T (°C)	Sliding velocity V (μm/s)	Final shear strain γ	Apparent compaction (mm)	Final steady state friction coefficient μ
MUS17	500	0.1	79.2	0.20	0.61
MUS18	500	3.7	63.7	0.18	0.68
MUS21	500	1	103.3	0.19	0.63
MUS04	500	1	ND	ND	ND
MUS05	300	1	36.9	0.12	0.70
MUS07	100	1	142.0	0.22	0.63–0.70
MUS11	500	1	133.4	0.19	0.89
MUS36	700	1	7.3	0.16	0.37

Normal stress-stepping experiments, $V = 1.0$ μm/s, $\sigma_{eff} = 20, 40, 60, 80, 100$ MPa

Experiment	Temperature T (°C)	Final shear strain γ	Final apparent compaction (mm)	Steady state friction coefficient μ	Notes
MUS01	20	29.1	0.08	0.43	
MUS02	150	25.0	0.08	0.43	
MUS03	500	28.6	0.15	0.51	Stick-slip
MUS06	400	28.7	0.08	0.60	
MUS08	300	ND	ND	0.54	
MUS09	600	27.4	0.06	0.74	
MUS12	500	27.8	0.06	0.76	Stick-slip
MUS16	100	30.3	0.22	0.38	
MUS22	700	31.7	0.14	0.55	Initial dilatation
MUS24	600	28.6	0.14	0.55	Initial dilatation
MUS28	225	22.6	0.16	0.37	
MUS29	500	28.5	0.01	0.49	Initial dilatation
MUS31	300	29.0	0.20	0.38	
MUS32	400	29.1	0.09	0.47	Initial dilatation
MUS33	500	33.5	0.14	0.53	Initial dilatation

Velocity-stepping experiments, $\sigma_{eff} = 100$ MPa, $V = 0.03, 0.1, 0.5, 1, 3.7$ μm/s

Experiment	Temperature T (°C)	Final shear strain γ	Final apparent compaction (mm)	Final steady state friction coefficient μ	Notes
MUS13	500	32.6	0.12	0.90	Stick-slip, initial dilatation
MUS14	300	37.0	0.14	ND	
MUS19	700	31.0	0.26	0.43	
MUS20	20	37.7	0.12	0.38	
MUS25	600	42.5	0.16	0.56	Initial dilatation
MUS26	150	42.2	0.11	0.46	
MUS30	500	44.8	0.14	0.62	Stick-slip, initial dilatation
MUS34	225	39.2	0.10	0.47	Initial dilatation
MUS35	400	40.2	0.16	0.54	

Compaction experiment, $\sigma_{eff} = 100$ MPa, $P_f = 100$ MPa

MUS23	700	0	0.11		

2.4. Data acquisition and processing

All temperature, fluid pressure, force, torque and rotational displacement signals were logged as a function of time, using a 16 bit A/D converter connected to a computer. Shear stresses and friction coefficients were calculated from the externally measured torque and axial force gauge signals using the method described below to correct for seal friction (Niemeijer et al., 2008). Slip displacements and rates were calculated directly from the measured rotary displacements making no correction for apparatus twist, as this effect was small compared to the displacements imposed.

Shear strains were calculated by dividing the measured rotary displacement by the initial gouge thickness, taken to be 0.62 mm in all tests. This was based on compaction experiments performed at room temperature and 100 MPa effective normal stress, showing that muscovite powder compacts to a porosity of ~27% under these conditions. This value agrees well with the 26–30%

initial porosity measured by Mariani et al. (2006) for muscovite gouges of the same grain size, cold-pressed in a die at room temperature. It is noted that subsequent hot-pressing of these samples by Mariani et al. (2006), for 30 h at 500–700 °C, reduced the porosity to 1–8%. In our shear experiments, however, the samples were pre-compacted under the deformation conditions for only ~45 min, resulting in a porosity at the beginning of each experiment that is most likely still rather close to the initial value, even at elevated temperatures. We, therefore, take 27% as the initial porosity of all our samples, implying a value for the sample thickness of 0.62 mm. During shear, porosity is further reduced, resulting in a decrease in sample thickness which might differ depending on temperature. Because of the uncertainties involved in precise determination of this thickness, we use the initial thickness for shear strain estimates. All reported shear strains, hence, are minimum values.

Typical results of a normal stress-stepping experiment showed a linear relation between the raw (uncorrected) shear stress and the effective normal stress data (Fig. 2), described as:

$$\tau_m = \mu_m \cdot \sigma_m + C_m = \tau_s + \tau_f \tag{1}$$

where τ_m is the measured shear stress, μ_m the slope of the shear stress-normal stress graph, σ_m the measured normal stress and C_m represents a constant. Since the shear stress is measured externally in our experimental set-up, the measured values τ_m are not only dependent on the shear and cohesive stresses supported by the simulated fault gouge τ_s, but also upon the frictional stress
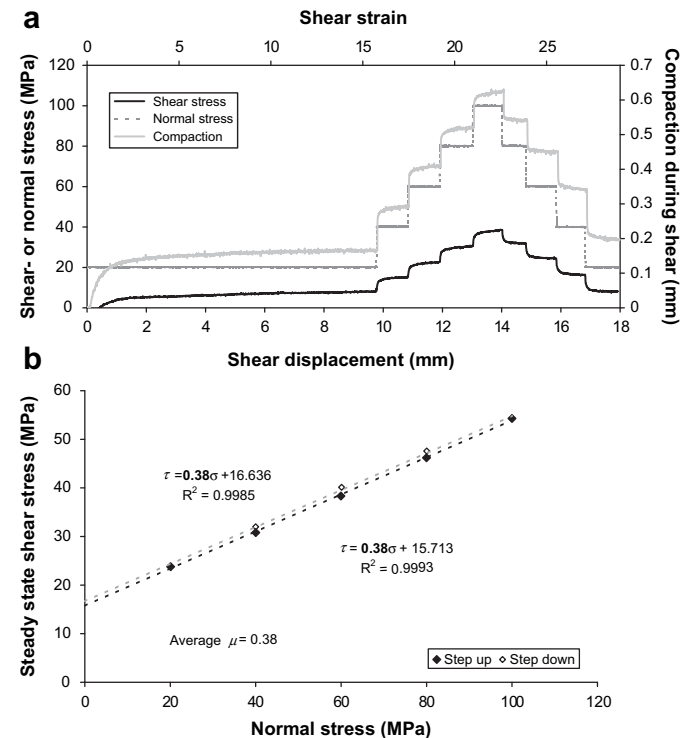
Fig. 2. Typical example of a normal stress-stepping experiment (MUS31), $T = 300$ °C, $P_f = 100$ MPa, $\sigma_{eff} = 20$–100 MPa, $V = 1.0$ μm/s and $\gamma = 29$. (a) Shear stress, normal stress and apparent compaction as function of shear displacement and shear strain. Note that the apparent compaction is not corrected for apparatus distortion. (b) Correlated shear stress vs. normal stress diagram. The slope of the linear best fit through the data points represents a measure for the mean steady state friction coefficient of the sample. The intercept of the linear best fit at zero effective normal stress is the effect of the friction of the O-ring seals and the confining rings (Niemeijer et al. (2008), see Section 2.4). These intercept values were used to correct the measured shear stresses obtained from velocity-stepping experiments.

contribution τ_f exerted by the O-ring seals on the pressure-compensated piston and by the confining rings surrounding the sample (Fig. 1c and d). Friction calibrations performed using an internal normal force gauge have shown that at measured normal stresses of 100 MPa the contribution of the O-ring friction to the normal stress is constant and negligible compared to the applied normal stress σ_m, so that the normal stress on the sample $\sigma_s = \sigma_m$. Therefore, the measured friction coefficient (μ_m in Eq. (1)) represents true sample behaviour $\mu_s = \tau_s/\sigma_s$ provided the O-ring contribution to the measured torque is independent of normal stress. We performed the following calibration experiments to allow meaningful processing of the data obtained.

In this procedure, two annular PEEK (PolyEtherEtherKetone) rings of ∼0.3 mm in thickness were inserted into the apparatus in the place of the usual fault gouge samples. Friction experiments were performed using these PEEK samples (i) with a stainless steel outer/inner confining ring, (ii) with a PEEK outer/inner confining ring, and (iii) without an outer confining ring. The frictional behaviour of the contact between the two solid PEEK samples was measured in all of these cases for effective normal stresses in the range 20–100 MPa. The data obtained show well-defined linear relations between shear stress and normal stress, indicating PEEK-on-PEEK friction coefficients μ_s in the range 0.03–0.06. No systematic change in μ_s was seen in relation to the type of inner/outer confining ring used (steel, PEEK or no ring), implying that the frictional forces generated by the confining rings are minor. The μ_s values 0.03–0.06 are low compared to the value of 0.1 (peek on peek) quoted by the manufacturer (see Niemeijer et al., 2008), but fit well with the low end of the range of 0.05–0.5 given in the literature (Burris and Sawyer, 2006a, 2006b; Theiler and Gradt, 2008). This agreement implies that the frictional forces caused by the seals and confining rings are unlikely to be significantly influenced by the normal stress. We, therefore, conclude that linear fits to the shear stress vs. normal stress data measured in our experiments on muscovite (Fig. 2) yield true friction coefficients μ_s for the fault gouge. This is consistent with previous conclusions based on experiments in the same apparatus by (Niemeijer et al., 2008).

From the data of Niemeijer et al. (2008), the cohesion C_s of our muscovite samples can be taken as near zero (Niemeijer et al., 2008, who measured 0.16 MPa for muscovite gouge), meaning that C_m in Eq. (1) is made up almost entirely of O-ring friction C_f. Values of C_m have been determined for every normal stress-stepping test performed. Although they show some variability (13–23 MPa), no systematic relationship with temperature was apparent. We, therefore, used the average value obtained for C_m (17 MPa) to correct the measured shear stress τ_m for O-ring and (minor) confining ring friction. Dividing the result by the applied effective normal stress σ_m (cf. Eq. (1)) then yields the internal friction coefficient of the sample:

$$\mu_s = \frac{\tau_m - C_m}{\sigma_m} \qquad (2)$$

Curves of corrected shear stress ($\tau_m - C_m$) vs. displacement can thus easily be recast into μ_s vs. shear strain γ curves for our samples.

Compaction and dilatation measurements were determined from the position of the Instron loading ram. Since the heated length of the loading pistons is very limited, we can assume that temperature does not influence elastic apparatus distortion. Axial machine distortion, therefore, depends only on normal stress. We did not correct for this. However, we compare measured compaction/dilatation data for different experiments only from the onset of shear deformation and at fixed effective normal stress. Any differences between experiments, therefore, reflect sample behaviour and are unrelated to apparatus behaviour.

2.5. Sample handling and microstructural methods

After the experiments, most samples broke into arc-shaped fragments during removal of the sheared gouge from the set-up. The fragments varied in size between 3 and 14 mm in arc length, by 3 mm wide and ∼0.5 mm thick. All were dried for ∼45 min at 60 °C after extraction. The dried samples were then vacuum impregnated with epoxy resin for about 15 min and left to dry for a period of 24 h. The impregnated fragments were finally sectioned normal to the shear plane and parallel to the shear direction, and polished. Mineral content and microstructure were investigated using a Scanning Electron Microscope (SEM) equipped with Energy Dispersive X-ray analysis system (EDX). Grain sizes and mineral fractions in the deformed samples were obtained from point counting analyses.

3. Mechanical and microstructural results

We performed 8 sliding experiments at fixed conditions, 14 normal stress-stepping experiments, 9 velocity-stepping experiments and 1 compaction experiment. The experiments and corresponding conditions are represented in Table 1.

3.1. Effect of shear strain

Fig. 3a and b shows the evolution of friction coefficient with shear strain for a number of samples deformed at 500 °C and at
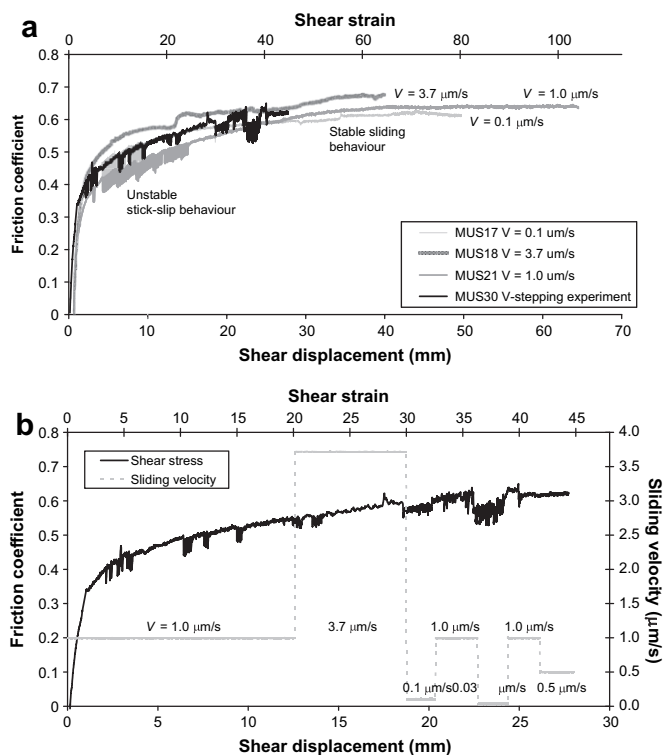

Fig. 3. (a) Friction coefficient vs. shear displacement (i.e. shear strain) obtained from three sliding experiments under constant conditions (non-stepping) at $T = 500$ °C, $P_f = 100$ MPa, $\sigma_{eff} = 100$ MPa and one velocity-stepping experiment under the same pressure and temperature conditions for comparison. The samples deformed at 0.1 and 1.0 μm/s show unstable stick-slip behaviour until sliding stabilizes at $\gamma = 16$ and $\gamma = 24$, respectively. The velocity-stepping experiment also shows unstable sliding in most steps, while the sample deformed at 3.7 μm/s exhibited stable sliding throughout the experiment. (b) Friction coefficient data from velocity-stepping experiment MUS30 compared with the steps in sliding velocity.

100 MPa effective normal stress. In the early stages of the experiments (γ up to 3), the friction coefficient strongly increased with shear strain, then gradually approached a steady state value of ~0.6 at γ of 35–40. The samples compacted more or less continuously during shear (Fig. 4a) with little effect of velocity (Fig. 4b). Stick-slip behaviour was observed in some experiments at 400 and 500 °C, but no systematic relationship with strain or velocity was found. Stick-slip was not observed in tests at temperatures outside this temperature range. Fig. 5 shows values of friction coefficient vs. shear strain at $\gamma > 7$, as obtained from a representative set of our velocity-stepping experiments. Note that data obtained at constant temperature (i.e. in a given stepping test) show a minor increase in friction coefficient with strain within the range $\gamma = 10$–35, and little effect of velocity.

Fig. 6a–d show the microstructures developed at shear strains of ~29, 40, 64 and 103, in samples deformed at 400 and 500 °C, 100 MPa fluid pressure and a sliding velocity of 1.0 μm/s. Of these samples, three were deformed under 100 MPa normal stress and one at 20–100 MPa in a normal stress-stepping experiment (MUS32). The microstructures developed at $\gamma = 29$ and $\gamma = 40$ at 400 °C (Fig. 6a, b and e) are rather similar. They show a muscovite foliation oblique to the shear direction and the presence of thin (~2 μm) anastomosing shear bands, dominantly in Y-shear orientation. Most muscovite grains have sizes of 5–20 μm, similar to the starting material and some grains show occasional folding or kinking. The thin bands contain grains of 1–2 μm, and are sometimes bounded by thicker (3–10 μm) zones of 1–4 μm size grains. Significant porosity is visible at the tips of the muscovite grains, which are often jagged and broken in appearance. About 5% quartz porphyroclasts (5–20 μm) are present, often showing extensional fractures.

a

b
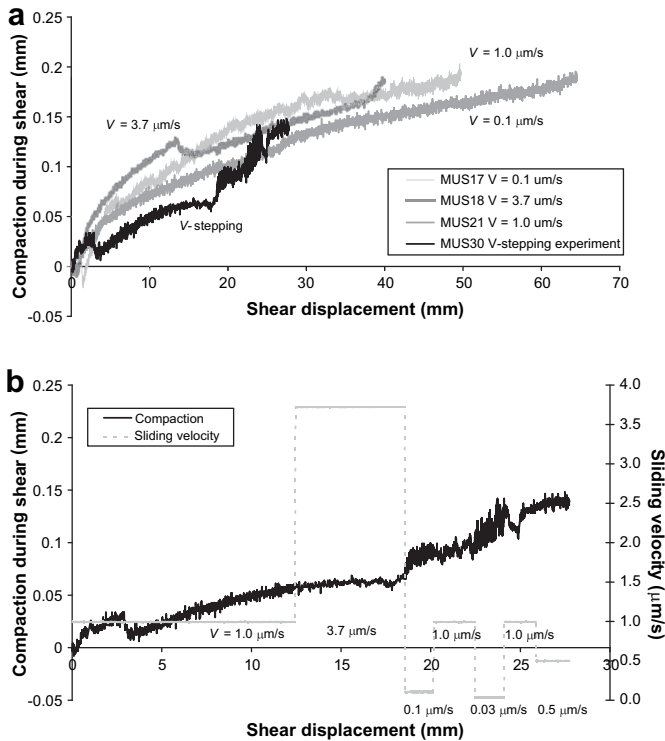
Fig. 4. (a) Compaction vs. shear displacement diagram obtained from the three constant velocity experiments and a single velocity-stepping experiment as in Fig. 3. Only the compaction recorded from the onset of shearing is indicated here, at constant effective normal stress of 100 MPa. The irregularities in the data signal are due to a low signal to noise ratio and are not related to stick-slip behaviour of the sample. (b) Compaction data from velocity-stepping experiment MUS30 compared with the steps in sliding velocity.
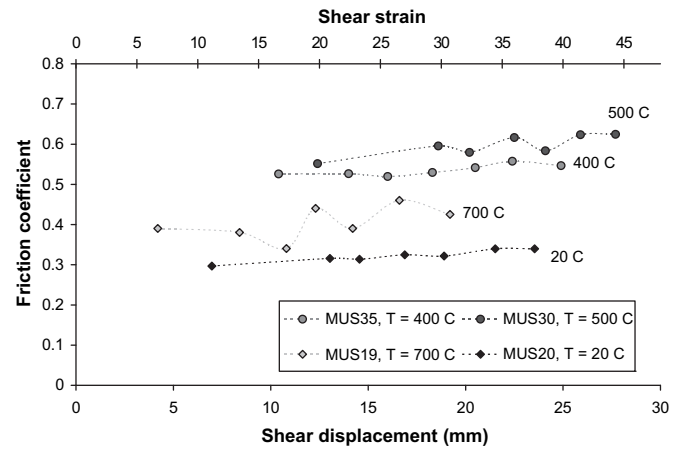

Fig. 5. Diagram illustrating the effect of shear strain on the coefficient of friction obtained from velocity-stepping experiments at different temperatures. At 700 °C, steady state shear stress levels were not reached within a single velocity step. The reported values for this temperature are only represented as an indication and should be considered with care.

The effect of shear strain can best be assessed using Fig. 6c and d for $\gamma = 64$ and $\gamma = 103$, both at 500 °C and similar normal stress and fluid pressure. Shear bands are wider now than seen at lower shear strain at 400 °C, and their width increases with strain, up to 20 μm in the sample deformed to $\gamma = 103$. The bands anastomose around dense lenses of coarser muscovite (Fig. 6f), show grain sizes <1 μm (Fig. 6g), and occupy roughly 20–35% of the gouge volume. The intervening lenses do not show a clear foliation, but do show local folding and kinking in the muscovite grains and have a grain size of 2–20 μm. The lenses also contain occasional quartz porphyroclasts with a grain size of 2–10 μm.

3.2. Effect of normal stress

Data on the measured shear stress, the effective normal stress and apparent compaction (uncorrected vertical displacement) vs. rotary displacement, obtained from a typical normal stress-stepping experiment (MUS31), are illustrated in Fig. 2a (see also Table 1). The corresponding shear stress vs. normal stress diagram, from which the mean steady state coefficient of friction is calculated, is shown in Fig. 2b. In individual stress steps, the shear stress initially increased rapidly, but reached steady state within ~1 mm of displacement (Fig. 2a). Also, the apparent compaction increased instantly when normal stress was stepped up, while an instant expansion occurred when normal stress was stepped down. Rough stiffness calibrations have shown that these vertical displacements were largely due to elastic distortion of the apparatus, though net compaction of the gouge was recorded at the end of the experiments (Table 1). We do not take the apparent compaction obtained from the normal stress-stepping experiments into account in the interpretation of our results, since we cannot correct accurately for apparatus stiffness. Nonetheless, friction coefficients obtained in the normal stress-stepping tests ranged from 0.37 to 0.60 depending on temperature (see Section 3.4).

Fig. 6a and b show microstructures of samples that reached different shear strains, at $T = 400$ °C, but that also differed in effective normal stress. The micrograph shown in Fig. 6a is obtained from an experiment in which the effective normal stress was stepped from 20 MPa to 100 MPa and back (in 20 MPa-steps). Fig. 6b represents a sample deformed at constant normal stress of 100 MPa. The microstructures of the two samples are rather similar (see also Section 3.1), hence, there seems to be no significant effect
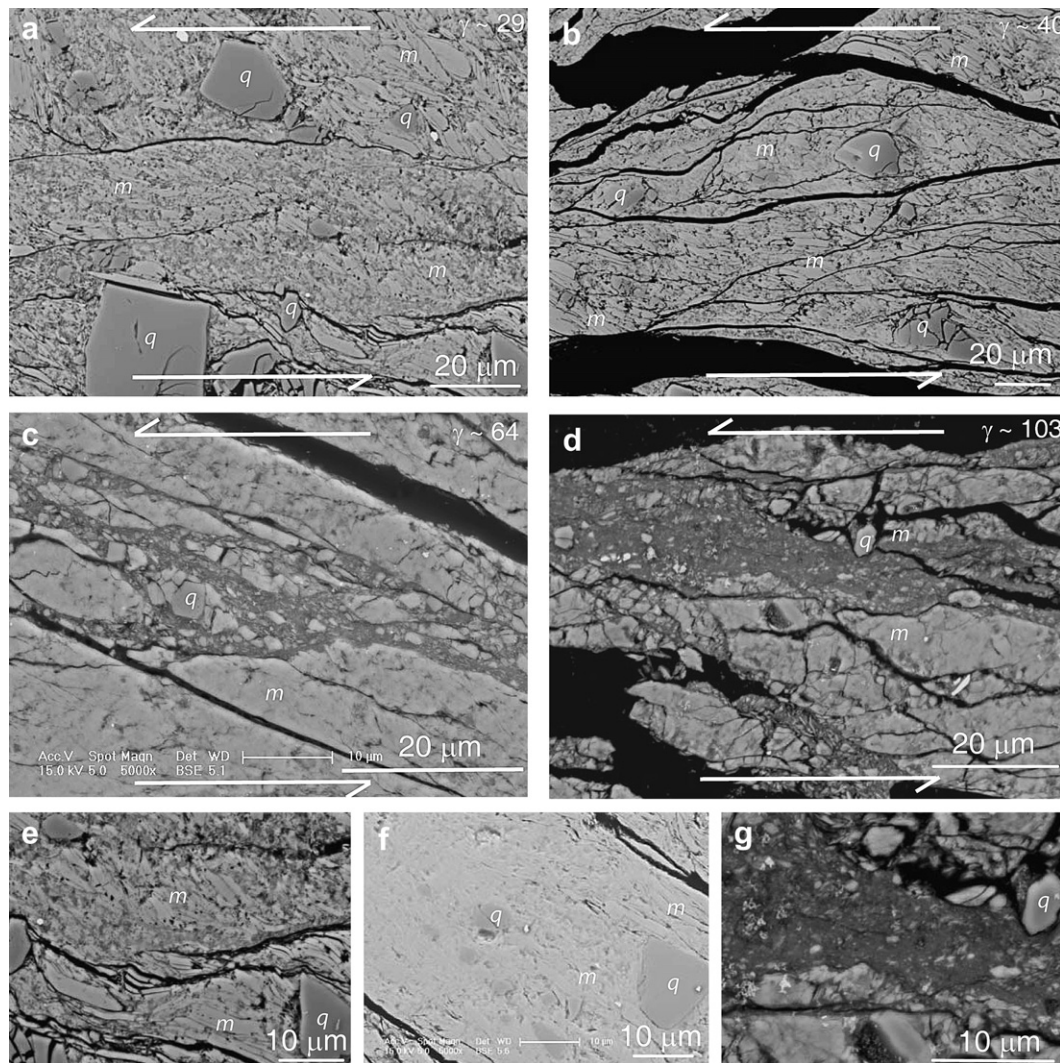
Fig. 6. SEM backscatter images showing the development of microstructure with increasing shear strain in samples deformed at 400 and 500 °C, 100 MPa fluid pressure and shear strain as indicated. The shear direction is sinistral and roughly horizontal. Note the progressive development of fine grained bands. At low strain, the muscovite grains (*m*) form a foliation oblique to the shear direction, while at high shear strain no foliation is observed and the bands anastomose around lenses of relatively less deformed material. Some quartz porphyroclasts (*q*) are present in all samples. (a) Obtained from normal stress-stepping experiment MUS32, $T = 400$ °C, $\sigma_{eff} = 20$–100 MPa and $V = 1.0$ μm/s. (b) Obtained from velocity-stepping experiment MUS35, $T = 400$ °C, $\sigma_{eff} = 100$ MPa and $V = 0.03$–3.7 μm/s. (c) Obtained from non-stepping experiment MUS18, $T = 500$ °C, $\sigma_{eff} = 100$ MPa and $V = 1.0$ μm/s. (d) Obtained from non-stepping experiment MUS21, $T = 500$ °C, $\sigma_{eff} = 100$ MPa and $V = 1.0$ μm/s. (e) Detail of Fig. (a) showing thin, fine grained bands. (f) Detail of a lense from sample MUS21. (g) Detail of Fig. (d) showing a thick, fine grained band.

of normal stress on the development of microstructures, at least not at 400 °C.

3.3. Effect of sliding velocity

From Figs. 3–5, it has already been noted that sliding velocity does not have an important effect on the mechanical behaviour of the gouges. This is largely confirmed in Fig. 7, where the steady state friction coefficients obtained in our velocity-stepping tests are explicitly plotted against sliding velocity. Clearly, there is no significant effect of velocity on friction coefficient at fixed temperatures up to 500–600 °C, though μ does increase with temperature (see Section 3.4). At 700 °C, the generally lower friction coefficient seems to peak at 1.0 μm/s, even though steady state shear stress levels were not reached under these conditions. We did not observe a systematic effect of sliding velocity on the compaction behaviour of the gouges (Fig. 4a and b).

The microstructures typifying samples deformed at constant sliding velocities ranging from 0.1 to 3.7 μm/s are illustrated in Fig. 8,

for $T = 500$ °C and for shear strains of about 63–79 (samples MUS17, 18 and 21, Table 1). The microstructures developed under these conditions are again characterized by fine grained, elongate lenses and oval clasts measuring typically 20–50 by 10 μm (Fig. 8a and c) consisting of often folded and kinked muscovites some 2–20 μm in length (Fig. 8b and d). In the SEM, the lenses show a low porosity and are separated by a through-going anastomosing network of ultra-fine grained ($\ll 1$ μm) bands, oriented parallel to and, though less well developed, at roughly 20–40° to the shear direction (Fig. 8a and c). These ultra-fine grained bands not only contain muscovite and (rare) quartz clasts ranging from $\ll 1$ to 10 μm in size, but also some fragments which are agglomerated grains and contain both muscovite and quartz (see detail image Fig. 6d).

On this basis, the main microstructural features do not seem to be strongly affected by sliding velocity. However, the dense muscovite lenses developed in the sample sheared at 0.1 μm/s show abundant rounded folds and only a few chevron type folds (Fig. 8b), whereas the sample sheared at high velocity (3.7 μm/s; Fig. 8d) shows more prominent chevron type folds and more signs of brittle deformation
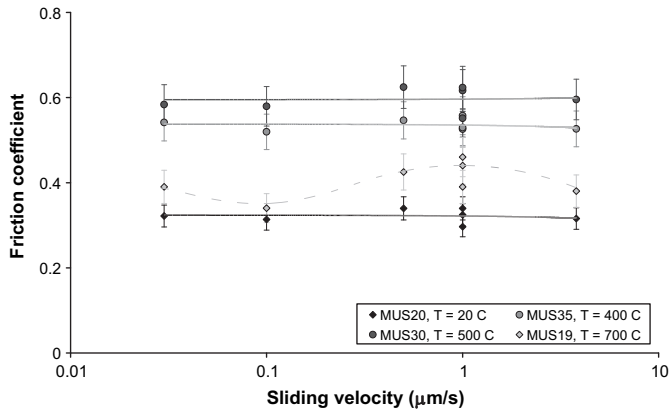
Fig. 7. Diagram illustrating the changes in friction coefficient with sliding velocity at different temperatures. At all temperatures but 700 °C, steady state shear stress levels, hence steady state friction coefficients, were reached within the amount of shear strain (1.5–4) obtained in individual steps.

at the hinges. Material sheared at 1.0 μm/s under similar conditions (MUS21) showed an intermediated microstructure.
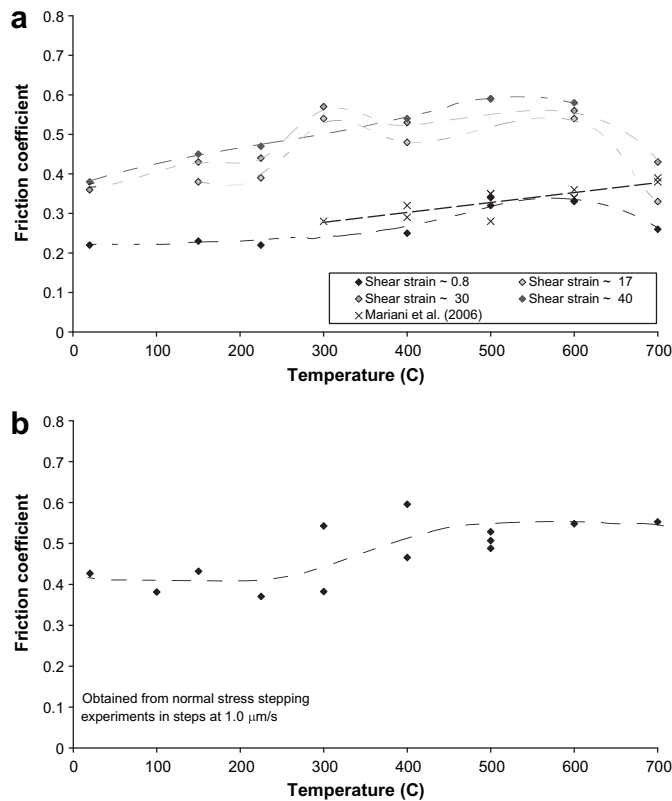
3.4. Effect of temperature

Fig. 9a shows the effect of temperature on friction coefficient as obtained at different shear strains from our velocity-stepping experiments at constant temperature. These data illustrate the significant increase in friction coefficient that occur up to $\gamma = 10$ and the steady state attained at shear strains of 30–40 (see Section 3.3). The steady state coefficient of friction increases from a mean value of 0.37 at 20 °C to 0.56 at 300 °C, remaining around this value up to 600 °C. At 700 °C, the coefficient of friction decreases again, to a mean value of 0.38 in the velocity-stepping tests. Fig. 9b shows the friction coefficient data obtained from the uncorrected normal stress-stepping experiments. These μ-values are not taken at a specific shear strain, but over the entire stepping sequence and thus incorporate an effect of shear strain. The absolute values shown in Fig. 9b increase from 0.38 at low temperature up to 0.60 at higher temperature. Although, these average values differ slightly from the friction coefficients obtained from the velocity-stepping tests, the trend in both data sets is very similar except at 700 °C. For comparison, the low shear strain data obtained at 400–700 °C by Mariani et al. (2006) are plotted in Fig. 9a. Note the good agreement with our low strain data, again except at 700 °C.

As illustrated in Fig. 10, the amount of apparent vertical compaction measured in the first portion of our velocity-stepping experiments, that is in the first 10 mm displacement at 1.0 μm/s, decreased slightly with increasing temperature up to 500 °C. The rate of compaction was highest in the early stages of shearing at 150–300 °C, but quickly decreased to a much lower rate at higher shear strain. At 500 and 600 °C (Figs. 4 and 10), limited initial dilatation is followed by gradual compaction at a rate that decreases with shear strain. The compaction behaviour at 700 °C differs from that at lower temperature; it reaches much higher values and appears to continue at a higher rate.
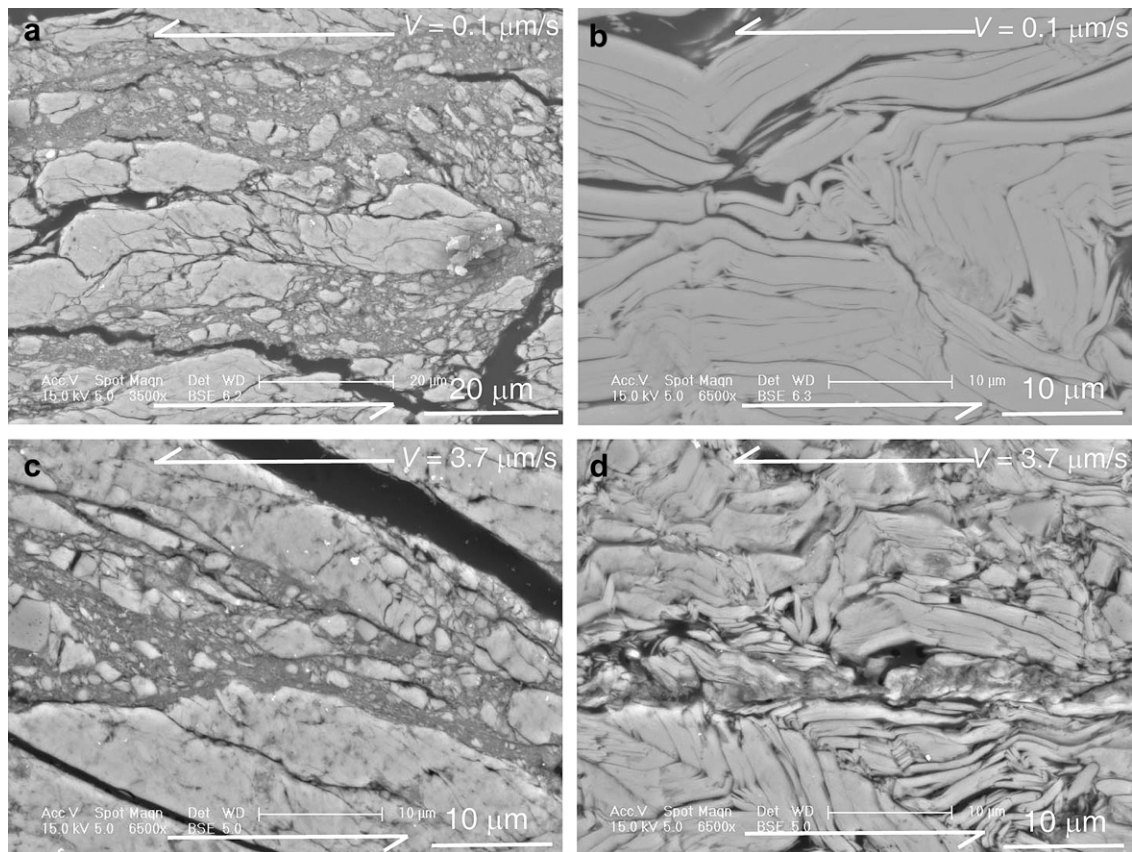

Fig. 8. SEM backscatter images showing the main structure developing in samples sheared at 500 °C, $\sigma_{eff} = 100$ MPa, $P_f = 100$ MPa and sliding velocities as indicated. The shear direction is sinistral and roughly horizontal. (a) Microstructure obtained from non-stepping experiment MUS17 ($\gamma = 79$), characterized by dense, elongate lenses, which are separated by a network of ultra-fine grained zones. (b) Detail of microstructure from sample MUS17, showing folding of the mica sheets inside one of the massive elongate lenses. (c) Obtained from non-stepping experiment MUS18 ($\gamma = 64$), which is very similar to Fig. (a). (d) Detail of microstructure from sample MUS18, showing an example of more chevron type folds that appear to be more prominent in samples sheared at 3.7 μm/s than at 0.1 μm/s.

Fig. 9. Diagrams showing the effect of temperature on friction coefficient. (a) Friction coefficients obtained at different shear displacements from velocity-stepping experiments at an applied normal stress of 100 MPa and a fluid pressure of 100 MPa. Data are corrected for ring- and seal friction as described in Section 2.5. (b) The friction coefficients obtained from normal stress-stepping experiments under $\sigma_{eff} = 20$–100 MPa, $P_f = 100$ MPa and at $V = 1.0$ µm/s. Note that these friction coefficients are mean values, obtained at different shear strains and from uncorrected shear- and normal stress data. They are used here to illustrate the trends rather than the absolute values.

The effect of temperature on the development of the micro-structure is illustrated in Fig. 11. The samples shown in the figure have shear strains from a relatively narrow range ($\gamma = 29$–42), except for the sample deformed at 500 °C ($\gamma = 64$). Fig. 11a and b show the microstructure of samples deformed at low temperature (MUS20, $T = 20$ °C; MUS26, $T = 150$ °C). These samples show
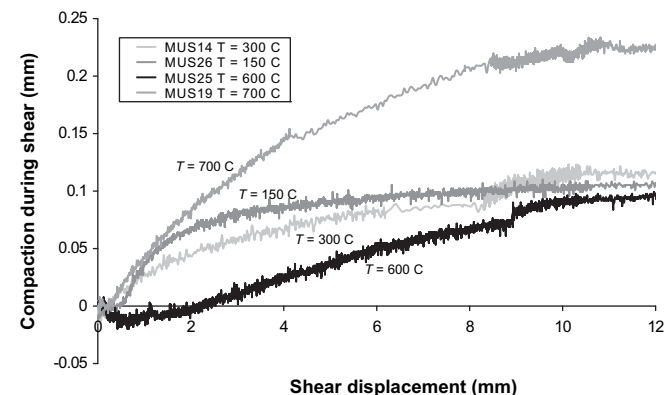
Fig. 10. Diagram showing the apparent compaction vs. shear displacement in the first portion of our velocity-stepping experiments, i.e., at $V = 1.0$ µm/s. Note the effect of temperature. At 600 °C the sample shows dilatation in the first 2 mm displacement, while the other samples continuously compact. The sample deformed at 700 °C shows most compaction.

thin shear bands (thickness <5 µm) roughly parallel and at a low angle to the shear direction, consisting of very fine material (<5 µm) separating lenses of larger muscovite grains (5–20 µm). Some of the lenses as well as some of the muscovite grains show elongated sigmoidal shapes. Quartz porphyroclasts up to 50 µm occur and often show extensional fractures.

Fig. 11c shows the microstructure of a sample sheared at 300 °C (MUS14). This micrograph displays dense looking lenses separated by shear bands that crosscut the sample. These fine grained zones vary in thickness from 5 to 50 µm and contain some large clasts (up to 40 µm) embedded in very fine (<2 µm) material. Some of these clasts appear to be clusters of agglomerated grains. At 500 °C (Fig. 11d), the microstructure is increasingly characterized by elongate lenses (20–50 by 10 µm) of fine folded and kinked grains (5–10 µm). The lenses are separated by a through-going anasto-mosing network of fine grained zones (grain size <1 µm), oriented at zero to roughly 30° to the shear direction.

In contrast to the samples deformed at lower temperature, the microstructure developed at 600 °C (Fig. 11e) displays no major zones with a reduced grain size. The structure is dominated by an oblique foliation defined by the muscovite grains oriented at an angle of roughly 20° to the sample boundary and shear direction. Quartz porphyroclasts are somewhat reduced in size (up to 5 µm) and some show of truncations suggestive of diffusive mass transfer processes such as pressure solution (Fig. 12).

The different shades in the SEM image of Fig. 13a and b at $\gamma = 7$ correspond to a different atomic number, indicative of different mineral phases or alteration. Quartz appears dark and muscovite light grey. The overall grain size of the material is small (<5 µm), but the larger mica grains define a wavy foliation parallel to the shear plane. In contrast to the foliation and banding developed at lower temperature, the foliation seen at 700 °C often shows sharp, wavy surfaces suggestive of slip surfaces. The quartz grains are fractured but form elongated, sigmoidal lenses with a stair-step-ping character and long, drawn-out tails not seen at 600 °C or below. A third phase is visible filling fractures plus voids in many quartz clasts (Fig. 13b and c). This other phase is present in amounts too small to be determined given the resolution of our EDX system. At 700 °C, clusters of agglomerated grains occur (Fig. 11f). The clusters are about 20–50 µm in size, while the grains in these agglomerates range from $\ll 1$ to 10 µm in diameter.

Fig. 13d shows a micrograph obtained from compaction experiment MUS23 ($T = 700$ °C) The mica grains are aligned normal to the compaction direction, some displaying intra-crystalline porosity. The contacts between the quartz and muscovite grains shows truncations and indentations and a number of muscovite grains appear corroded.

4. Discussion

4.1. Deformation mechanisms and gouge evolution

The trends in frictional and volumetric behaviour seen with changing conditions, notably strain and temperature, can be explained in terms of the microstructures developed in the sheared gouges. A characteristic element of the microstructure is the generally reduced size of the muscovite grains compared to the starting grain size, the angular shapes of many of the fine grains, and the progressive development with strain of anastomosing (ultra) fine grained bands parallel to the shear plane at least up to 500 °C. From these features, from the jagged ends of the coarser muscovites, and from the clearly fractured quartz clasts, we conclude that cataclasis is the grain size reducing mechanism at 20–500 °C. The fine grained bands suggest a tendency for locali-zation. Cataclasis generally produces a broadening grain size
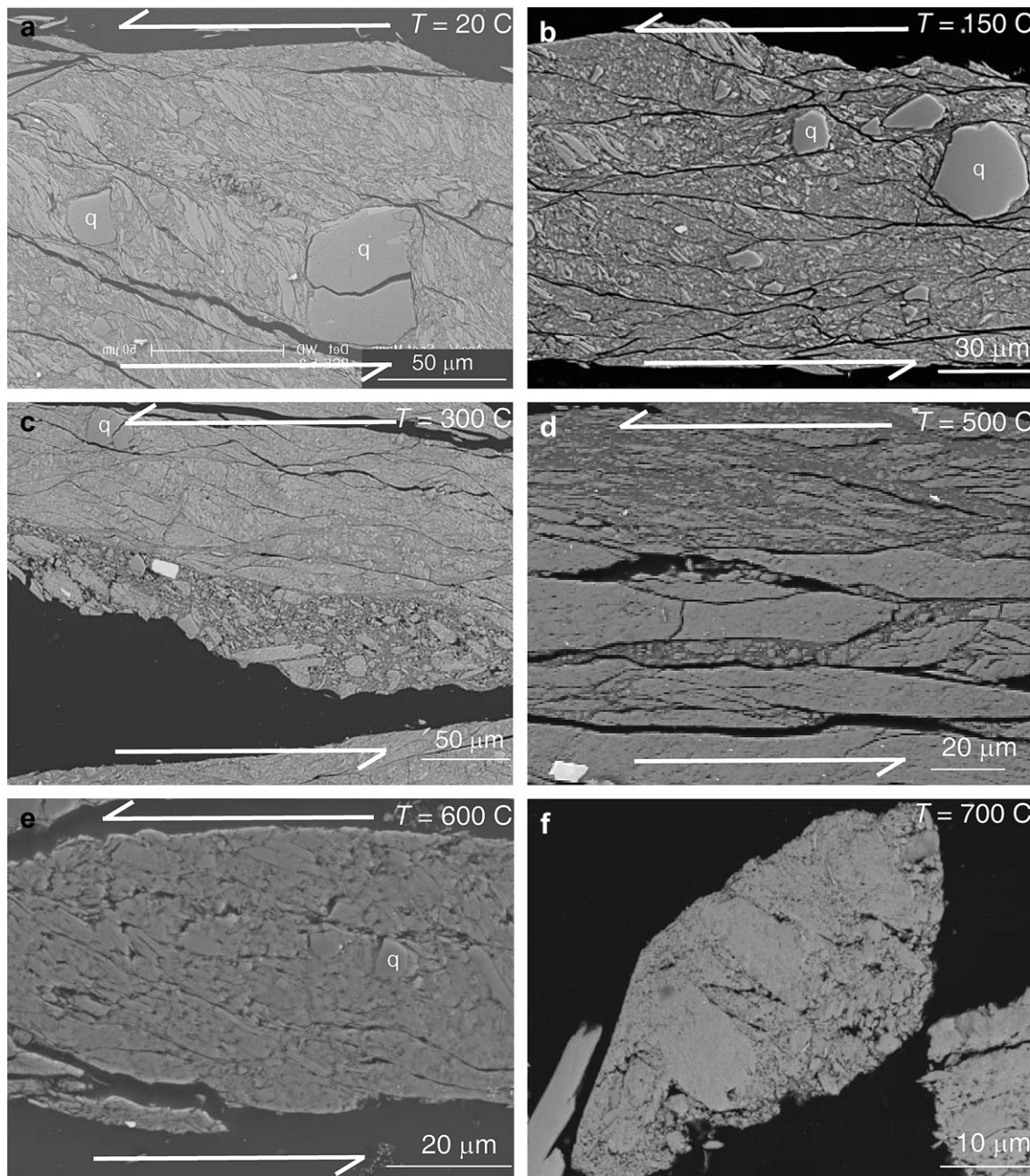
Fig. 11. SEM backscatter images showing the effect of temperature on the microstructure at 100 MPa fluid pressure. Most fault gouges have fragmented after retrieval from the shear apparatus. The shear direction is sinistral and roughly horizontal and temperature is as indicated. (a) Microstructure obtained from velocity-stepping experiment MUS20, $\sigma_{eff} = 100$ MPa, $V = 0.03$–3.7 μm/s and $\gamma = 38$ showing large quartz porphyroclasts (q) and fractured grains. The mica grains (m) define an oblique foliation and the overall structure is cross cut by fine grained shear bands. (b) Structure obtained from velocity-stepping experiment MUS26, at conditions similar to (a), only at a different temperature. (c) Structure obtained from velocity-stepping experiment MUS14, $\sigma_{eff} = 100$ MPa, $V = 0.03$–3.7 μm/s and $\gamma = 37$, showing denser lenses, surrounded by more fine grained zones, widening with increasing shear strain. (d) Micrograph from the sample deformed in non-stepping experiment MUS18, at $\sigma_{eff} = 100$ MPa, $V = 3.7$ μm/s and $\gamma = 64$. This structure again shows dense lenses, surrounded by a network of fine grained bands. (e) Structure obtained from normal stress-stepping experiment MUS24, sheared at $\sigma_{eff} = 20$–100 MPa, $V = 1.0$ μm/s and $\gamma = 29$, showing no major grain size reduction compared to the starting material. The muscovite grains define a strong, foliation oblique to the shear direction. (f) Fragment obtained from sample MUS19, $\sigma_{eff} = 100$ MPa, $V = 0.03$–3.7 μm/s and $\gamma = 31$ showing agglomerated muscovite grains.

distribution (Rawling and Goodwin, 2003; Sammis et al., 1987), which results in a decrease in porosity, an increase in density and hence on-going compaction (Saileswaran and Panchanathan, 1973), in agreement with our findings (Fig. 4). Such compaction will in general increase friction coefficient due to an increasing dilatation angle (Niemeijer and Spiers, 2006).

In an attempt to explain the strain hardening behaviour seen in our experiments, we infer that with increasing strain, both pervasive and localized cataclasis, and related compaction, first result in hardening, which leads to widening of the finer anastomosing bands (cf. Scruggs and Tullis, 1998), at the cost of the low strain lenses. Steady state is then approached as the microstructure becomes dominated by the development of a continuous network of fine grained bands and oblique foliation. The increase in width of these fine grained cataclastic bands with temperature appears to be associated with an increase in friction coefficient (at high strain), perhaps implying that compaction and hence hardening are promoted by thermally activated
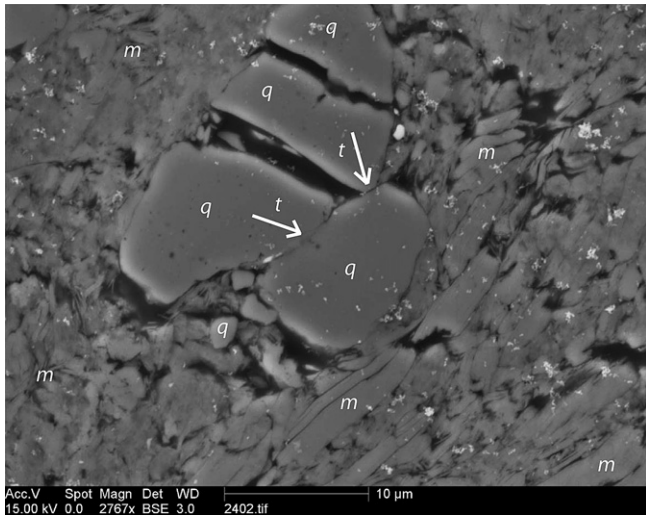
Fig. 12. SEM backscatter image obtained from normal stress-stepping experiment MUS24 ($T = 600\,°C$, $\gamma = 29$). The quartz porphyroclasts (q) in the micrograph is fractured and shows truncations (t), suggestive of the operation of mass transfer processes. The rest of the structure consists of fine muscovite (m) grains. No marked reaction products due to the breakdown of muscovite + quartz are visible at the muscovite–quartz interfaces.

diffusive or plastic flow processes in the bands. The coarse lenses show folded and kinked muscovite grains indicative of active crystal plastic mechanisms. Observations on these mechanisms, however, are not diagnostic enough to draw conclusions

regarding the contribution of plastic deformation to the bulk mechanical behaviour.

Upon reaching 600 °C, the fine grained bands become a less prominent microstructural feature than at 20–500 °C (Fig. 11e), though the overall microstructure remains that of a gouge with a grain size reduced compared to that of the starting material. The strength of the gouge is still directly dependent on normal stress (as in Fig. 2), demonstrating that there was no major change in deformation mechanism going from low to high temperature at the strain rates applied in this study. Moreover, the friction coefficient at 600 °C is not dissimilar from that at 400 and 500 °C, suggesting that the difference in microstructure (homogeneous matrix vs. broad bands, respectively – see Figs. 11e and 6) does not result in a difference in bulk mechanical behaviour.

At 700 °C, the chemical variations visible on the SEM images (Fig. 13a–c) together with the corroded appearance of muscovite grains (Fig. 13d) suggest that under these conditions muscovite breakdown reactions may have played a role. These then would have changed the gouge such that a decrease in friction coefficient resulted, from 0.56 at 600 °C to 0.38 at 700 °C. The sigmoidal quartz clasts are mostly fractured and a number of these cracks appear to have been filled by a different phase, which also forms long (50–100 μm) tails (Fig. 13a–c) and might be indicative of partial melting of the gouges.

With respect to the <10% quartz present in our samples, we note the following. At all observed scales, the quartz grains occurred as isolated clasts and did not form a connected network. Niemeijer and Spiers (2005) showed that the presence of up to 20% of halite in
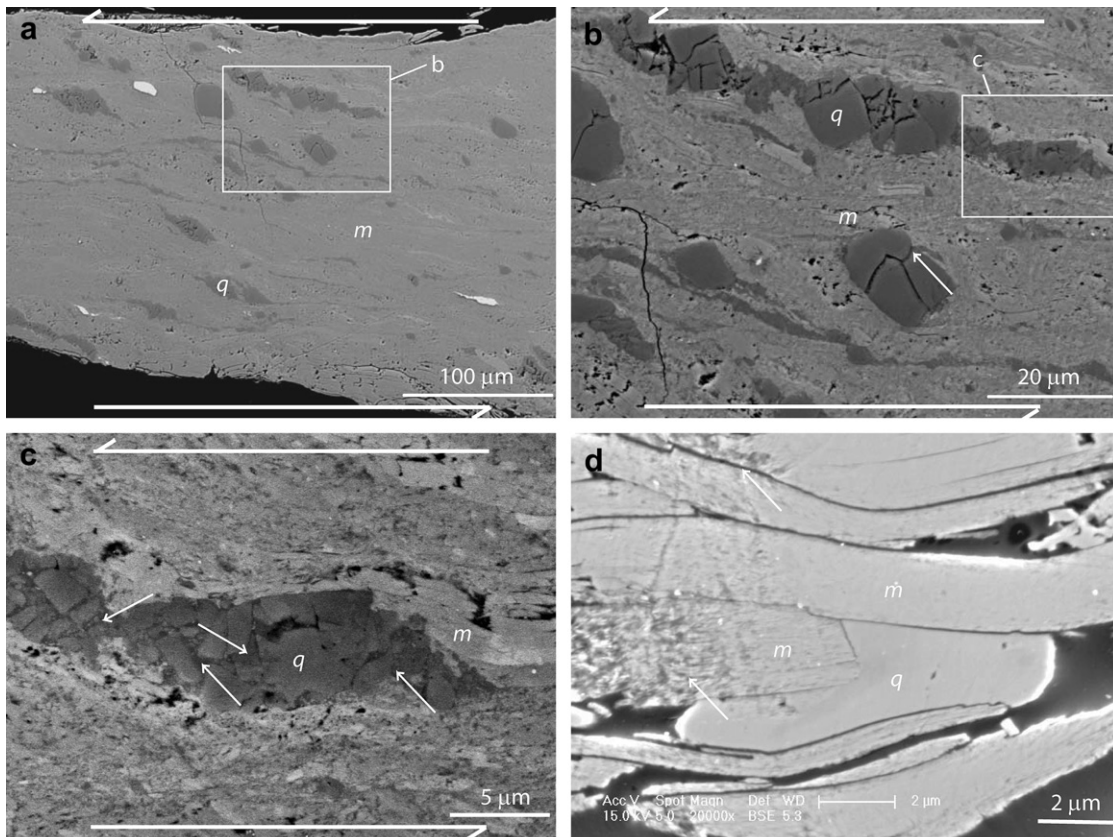
Fig. 13. SEM backscatter images showing the microstructure of muscovite gouge at 700 °C. The shear direction is roughly horizontal and the shear sense is sinistral. Figures a–c are obtained from non-stepping experiment MUS36 sheared at $T = 700\,°C$, $V = 1.0\ \mu m/s$ and $\gamma = 7$. (a) Micrograph showing a dense, foliated microstructure with muscovite (light grey, m), quartz (dark, q) and a few impurities (white). Some grains are fractured and the overall grain size appears smaller than the starting grain size, though some large muscovites remain. (b) Detail from (a) showing the altered appearance of fractured quartz grains. A possible third phase filling the cracks is indicated with an arrow. (c) Detail from (b). Note the third phase present between the fractured quartz grains, indicated with arrows, possibly due to partial melting of the sample. (d) Micrograph from compaction experiment MUS23. The microstructure has not been sheared, and no foliation or shear bands have developed. Some grains appear corroded, possibly due to chemical alteration and the grain contacts are clearly visible.

a muscovite fault gouge results in a slightly higher shear stress, without changing the mechanical behaviour and velocity-dependence of the mixture. Assuming that our isolated quartz grains do not behave much different in the muscovite gouge than the low % of halite of Niemeijer and Spiers, we infer that the presence of quartz in our samples did not strongly influence the measured friction coefficients.

4.2. Stability of muscovite: decomposition vs. melting

Dehydroxylation reactions of dry muscovite can be expected to start around 400 °C. These reactions, however, are substantially inhibited by applying a pore fluid pressure in the order of 100 MPa (Mariani et al., 2006). Since we have applied 100 MPa fluid pressure in all experiments, it is unlikely that muscovite dehydroxylation played an important role in our experiments.

At around 600 °C and fluid pressures of 100 MPa, decomposition of muscovite plus quartz may take place following the reaction (Chatterjee and Johannes, 1974): Muscovite + Quartz → K-feldspar + Andalusite + Water. Since our samples contain <10% of quartz, we expected to see reaction products around the quartz grains in samples deformed at 600 °C. However, no evidence for the decomposition or reaction of muscovite and quartz was found (see Fig. 12). Around 700 °C and water pressures of 100 MPa, decomposition of muscovite occurs following the reaction (Chatterjee and Johannes, 1974): Muscovite → K-feldspar + Corundum + Water. Our compaction experiment at 700 °C (MUS23) showed altered/corroded muscovite grains, indicating that chemical alteration of the muscovite indeed occurred (Fig. 13d). Although the different shades on the SEM images (Fig. 13a–c) from the sample sheared at 700 °C suggest the presence of new mineral phases, the limited amount of reaction product did not allow meaningful EDX analysis, given the resolution of our set-up. Mariani et al. (2006) performed detailed TEM analysis on muscovite samples deformed at this high temperature and reported various reaction products following the reaction: Muscovite → K-feldspar + Biotite + Mullite + Water. The exact decomposition reaction is strongly influenced by the chemical composition of the starting material. For example, Na-for-K substitution reduces the temperature stability of white micas (Deer et al., 1962). However, K-feldspar is produced in all decomposition reactions of muscovite at this high temperature. It is, therefore, not unlikely that K-feldspar was formed.

The presence of quartz in combination with muscovite and water lowers the melting temperature of the aggregate to ∼700 °C at 5 kbar pressure (Huang and Wyllie, 1974), suggesting an even lower melting temperature under the conditions reached in this study. It is thus possible that the phase in the cracks (Fig. 13a–c) is partial melt lubricating the grain contacts. Previous high-velocity friction experiments on fault gouge have shown that the presence of a small amount of melt reduces the friction of a fault surface significantly (Di Toro et al., 2006).

4.3. Comparison with previous work

The coefficient of friction for muscovite obtained in this study was found to be 0.37 at room temperature, which is in reasonably good agreement with values reported from previous room temperature experiments on muscovite fault gouge: 0.38 (Scruggs and Tullis, 1998), 0.42 (Moore and Lockner, 2004; Morrow et al., 2000) and 0.4 (Mares and Kronenberg, 1993). Scruggs and Tullis (1998) sheared wetted muscovite gouge without fluid pressure under 25 MPa effective normal stress up to shear displacements up to 150–200 mm. Moore and Lockner (2004) and Morrow et al. (2000) performed experiments on wet muscovite fault gouge at low shear strains and Mares and Kronenberg (1993) deformed dry,

single crystals of muscovite under different pressures. The difference between the values of the friction coefficients resulting from the various studies is probably due to the different experimental set-ups, the presence or absence of pore fluid, use of different starting materials, and variations in shear strains reached. Despite these differences, all reported friction coefficients for wet muscovite at room temperature fall in the range $\mu = 0.39 \pm 0.03$.

Strain hardening behaviour is often observed in experiments on muscovite and other phyllosilicates (Logan and Rauenzahn, 1987; Mariani et al., 2006; Moore and Lockner, 2004; Moore and Rymer, 2007; Morrow et al., 2000; Rutter and Maddock, 1992; Rutter et al., 1986). We attribute the strain hardening behaviour observed at $\gamma < 10$ in our experiments to pervasive cataclasis coupled with the development of cataclastic shear bands (made of fine grained material) and an oblique foliation, cf. Scruggs and Tullis (1998). We suggest that the hardening is caused by grain size reduction and associated compaction, leading to a change in dilatation angle and an increase in friction coefficient. These bands are at an angle of roughly 20–40° to the shear direction, regardless of shear strain and normal stress, suggesting that they are dynamically stable. The bands widen at the cost of the lenses, until a steady state shear stress is reached.

We turn now to the effect of temperature on μ. Moore and Lockner (2004) observed a positive correlation between the value for the coefficient of friction of wet sheet silicate gouges at room temperature and the electrostatic separation energy of the minerals. Sheets silicates with a relatively strong bonding between the individual sheets are likely to have a higher coefficient of friction than those with a weak bonding between the sheets. These authors infer that water forms thin, structured films between the sheet surfaces. The polar water molecules are bonded to the plate surfaces in proportion to the mineral's surface energy. The friction coefficient of the sample reflects either the strength of the bonding between the water and the different mineral surfaces or the stresses required to shear through these water films themselves. Consequently, the coefficient of friction of a given sheet structure mineral depends on the properties of the mineral surfaces and/or the properties of the fluid phase and changes therein. An increase in temperature could drive the adsorbed water off the mineral surfaces, resulting in an increase in friction coefficient, as previously observed in serpentine gouges (Moore et al., 1997). Although the friction coefficient of our samples increases with temperature, the constant fluid pressure of 100 MPa is likely to maintain the presence of thin water films between the sheet surfaces. We, therefore, attribute the observed change in friction coefficient to the development of the observed networks of shear bands rather than to a change in the bonding between the pore water and the mica surfaces.

Mariani et al. (2006), who performed direct shear (saw-cut) experiments on simulated muscovite gouge at temperatures of 300–700 °C, reported friction coefficients that are in good agreement with our absolute values for μ at $\gamma < 10$ (see Fig. 9a). Since the samples deformed by Mariani et al. (2006) have a very-low (<9%) starting porosity it is unlikely that compaction during shear attributed to the observed strain hardening in their experiments. Mariani et al. inferred that misaligned mica grains can serve as obstacles to sliding, causing the hardening. They suggest that as the microstructure evolves with shear strain and more and more grains align themselves, the hardening rate is reduced and a steady state shear stress may be reached. Because of the low strains attained in the experiments of Mariani et al., such steady state was never reached in their tests, but is clearly approached in our experiments. However, the microstructures of our samples do not show an evolving alignment of muscovite grains parallel to the shear direction. Rather, a dynamically stable microstructure consisting of

Y-shear bands of cataclastic material and an oblique foliation developed. This suggests that at low shear strain, in samples where little syn-deformational compaction occurs (cf. Mariani et al., 2006), misaligned grains may result in hardening of the gouge, whereas at higher shear strains in gouges that densify during deformation (this study), cataclasis and the formation of fine grained bands can explain the observed strain hardening behaviour.

Sliding velocity and thus shear strain rate did not significantly effect the friction coefficients under the explored conditions in good agreements with Mariani et al. (2006) and Niemeijer and Spiers (2005). However, a change from rate-independent to rate-dependent behaviour was reported at shear strain rates of 10^{-6} s^{-1} by Mariani et al. (2006) obtained during both constant displacement rate and relaxation tests, which is at slower rates than the 10^{-5} to 10^{-3} s^{-1} applied in the present study. This rate-dependent behaviour was attributed to viscous glide of basal dislocations becoming competitive at low strain rates, but was not seen in our faster experiments. Stick-slip behaviour at temperatures of 400–500 °C was observed by Mariani et al. (2006), and confirmed under similar pressure and temperature conditions in our experiments.

Mares and Kronenberg (1993) performed shortening experiments on single crystals of muscovite using a Heard-type triaxial gas apparatus at temperatures of 20–400 °C. These authors suggest that deformation of muscovite crystals may occur by dislocation glide at 45° to (001), kink generation at 0° to (001) or fracture at 90° to (001). They observed evidence of dislocation glide in samples deformed at 45° to (001) at temperatures of 20, 200 and 400 °C. Evidence for plastic deformation in muscovite single crystals at room temperature and pressure has been previously reported during basal plane slip (Meike, 1989). Our results, including those at higher temperature also show some evidence of ductile deformation, notably the folding of muscovite grains, but always subordinate compared to the role of cataclasis. This is most likely due to the relatively high strain rates used in our experiments. Moreover, the reported observations of plastic deformation in muscovite at room temperature were obtained from experiments on single crystals (Mares and Kronenberg, 1993; Meike, 1989), whereas our samples consist of fine grained fault gouge. Mariani et al. (2006) observed plastic deformation in muscovite fault gouge at elevated temperatures and low strain rates. We, therefore, suggest that the deformation of fine grained fault gouge of grain sizes used here was by cataclasis and grain boundary sliding at high strain rates, while plastic mechanisms may control deformation at low strain rates or in coarser material, less likely to slide and fracture.

At 700 °C, muscovite breakdown reactions result in a different mechanical behaviour of the gouges and associated development of modified microstructures. Mariani et al. (2006) observed at 700 °C a sudden weakening, similar to our results but also a change from rate-independent to rate-dependent behaviour. However, they observed the growth of K-feldspar grains as a result of the chemical breakdown of the muscovites and did not observe evidence for partial melting. We attribute this difference in chemical behaviour at 700 °C to the relatively high percentage of quartz impurities in our samples (<10% compared to <1%). These quartz impurities reduce the melting temperature of our samples to ∼700 °C (Huang and Wyllie, 1974), while the melting temperature in the samples of Mariani et al. is well outside the range of their experimental conditions.

4.4. Implications for natural fault zones

Our experiments indicate that muscovite fault gouges strengthen with increasing temperature up to 600 °C, showing an increasing in friction coefficient from 0.37 to 0.56. In other words,

muscovite gouge becomes increasingly more resistant to sliding with increasing temperature at the sliding velocities studied (strain rates 10^{-5} to 10^{-3} s^{-1}). In order to obtain a first-order assessment of the importance of muscovite strength in crustal faults, we used the data presented in Fig. 9a to construct a frictional strength profile for the crust that allows comparison with Byerlee's Rule (Fig. 14). For the strain rates applied in our study, the shear strength of muscovite appeared independent of sliding velocity, hence we did not include a rate effect on μ beyond the range of sliding velocities investigated. It is noted, however, that rate-dependent behaviour, was observed by Mariani et al. (2006) for strain rates lower than ours, but only at 700 °C, i.e., at depths 20–45 km depending on geothermal gradient (lowermost part of our profile). It is unclear if and to what extent the rate-dependent behaviour of Mariani et al. occurs at slow strain rates at lower temperature than 700 °C.

We calculated our crustal strength profile using the approach previously used by Bos and Spiers (2002) and Niemeijer and Spiers (2005). We assumed a geothermal gradient of 30° km^{-1} and a surface temperature of 25 °C, an average crustal density of 2.7 gcm^{-3}, and a Byerlee friction coefficient of 0.75. A frictional strength profile corresponding to $\mu = 0.2$ is added to represent the strength expected for the San Andreas fault zone on the basis of heat flow measurements (Lachenbruch and Sass, 1980). The crystal plastic flow strength of muscovite is added (Fig. 14) following (Kronenberg et al., 1990) for shear strain rates of 10^{-14}, 10^{-12}, and 10^{-10} s^{-1} and assuming an activation enthalpy of 270 kJmol^{-1} (Mariani et al., 2006). The flow strength of quartz is added since this is lower than the flow strength of muscovite under low-crustal conditions (Fig. 14) following an empirical equation for dislocation creep (Gleason and Tullis, 1995).

The shear strength of muscovite gouge inferred from our experimental data, at depths of 5–10 km, is 30–70 MPa, while a strength of 10–20 MPa is implied for the San Andreas fault zone (Lachenbruch and Sass, 1980). Based on these results, it seems
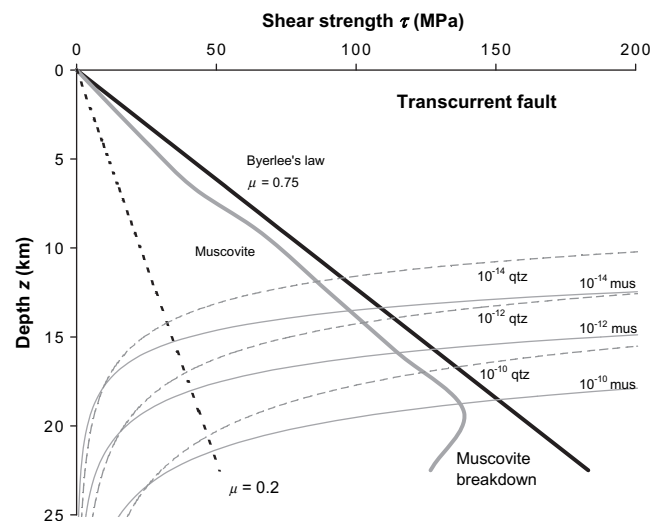
Fig. 14. Crustal strength profile comparing Byerlee's Rule with the frictional strength profile for muscovite, drawn using data presented in Fig. 9a. We assumed a geothermal gradient of 30° Ckm^{-1} and a surface temperature of 25 °C, an average crustal density of 2.7 gcm^{-3}, and a Byerlee friction coefficient of 0.75. The frictional strength profile corresponding to $\mu = 0.2$ is added to represent the strength expected for the San Andreas fault zone on the basis of heat flow measurements (Lachenbruch and Sass, 1980). The plastic flow strength of muscovite is added following Kronenberg et al. (1990) for various strain rates assuming an activation energy of 270 kJmol^{-1} after Mariani et al. (2006). The plastic flow strength of wet quartz is added following Gleason and Tullis (1995), since it is lower than the flow strength of muscovite under low-crustal conditions.

unlikely that the presence of muscovite alone, with the rate-independent frictional strength as taken in our study, can account for the inferred weakness of large scale crustal fault zones. Muscovite, however, shows stick-slip behaviour, which is the laboratory equivalent of earthquakes, at temperatures between 400 and 500 °C, corresponding to a depth of 13–17 km in a transcurrent fault zone. This unstable sliding behaviour might be of some significance in controlling fault behaviour towards the base of the seismogenic zone.

5. Conclusions

The present study aimed to determine the frictional behaviour of simulated muscovite fault gouge at high shear displacements and under hydrothermal conditions in the temperature range 20–700 °C, at shear strain rates $\sim 10^{-5}$ to 10^{-3} s^{-1}. The following conclusions were reached:

(1) all our samples showed strong strain hardening at low shear strains, followed by a more gradual increase in strength, until steady state was reached. The steady state coefficient of friction increased from 0.37 at room temperature to 0.56 at 300 °C, remaining around this value up to 600 °C. At 700 °C, the coefficient of friction decreased again, to a value of 0.38;

(2) all samples showed substantial grain size reduction at T up to 600 °C due to pervasive and localized cataclasis, which resulted in continuous compaction and hardening of the gouge. This hardening is due to the progressive development of an anastomosing network of fine grained, cataclastic shear bands, gradually widening and hardening. Coarse grained relict lenses between the cataclastic bands show folded and kinked muscovite grains indicative of active ductile mechanisms;

(3) due to the presence of quartz impurities ($<$10%) in the gouge it is possible that partial melting occurred at 700 °C;

(4) on the basis of our results, it seems unlikely that the presence of muscovite can significantly contribute to the long-term weakness of large scale crustal fault zones, unless its strength dramatically decreases with decreasing sliding velocity or shear strain rate.

Acknowledgements

References

Arancibia, G., Morata, D., 2005. Compositional variations of syntectonic white-mica in low-grade ignimbritic mylonite. Journal of Structural Geology 27, 745–767.

Balfour, N.J., Savage, M.K., Townend, J., 2005. Stress and crustal anisotropy in Marlborough, New Zealand: evidence for low fault strength and structure-controlled anisotropy. Geophysical Journal International 163, 1073–1086.

Blanpied, M.L., Lockner, D.A., Byerlee, J.D., 1995. Frictional slip of granite at hydrothermal conditions. Journal of Geophysical Research 100, 13045–13064.

Bos, B., Peach, C.J., Spiers, C.J., 2000. Slip behavior of simulated gouge-bearing faults under conditions favoring pressure solution. Journal of Geophysical Research 105, 16699–16717.

Bos, B., Spiers, C.J., 2000. Effect of phyllosilicates on fluid-assisted healing of gouge-bearing faults. Earth and Planetary Science Letters 184, 199–210.

Bos, B., Spiers, C.J., 2001. Experimental investigation into the microstructural and mechanical evolution of phyllosilicate-bearing fault rock under conditions favouring pressure solution. Journal of Structural Geology 23, 1187–1202.

Bos, B., Spiers, C.J., 2002. Frictional-viscous flow of phyllosilicate-bearing fault rock: microphysical model and implications for crustal strength profiles. Journal of Geophysical Research 107, 2028. doi:10.1029/2001JB000301.

Burris, D.L., Sawyer, W.G., 2006a. Improved wear resistance in alumina-PTFE nanocomposites with irregular shaped nanoparticles. Wear 260, 915–918.

Burris, D.L., Sawyer, W.G., 2006b. A low friction and ultra low wear rate PEEK/PTFE composite. Wear 261, 410–418.

Byerlee, J., 1990. Friction, overpressure and fault normal compression. Geophysical Research Letters 17, 2109–2112.

Byerlee, J.D., 1978. Friction of rocks. Pure and Applied Geophysics 116, 615–626.

Carpenter, B.M., Marone, C., Saffer, D.M., 2009. Frictional behavior of materials in the 3D SAFOD volume. Geophyscial Research Letters 36. doi:10.1029/2008GL036660.

Chatterjee, N.D., Johannes, W., 1974. Thermal stability adn standard thermodynamic properties of synthetic 2M1-muscovite, KAl2[AlSi3O10(OH)2]. Contributions to Mineralogy and Petrology 48, 89–114.

Chester, F.M., 1995. A rheologic model for wet crust applied to strike slip faults. Journal of Geophysical Research 100, 13033–13044.

Collettini, C., Barchi, M.R., 2002. A low-angle normal fault in the Umbria region (Central Italy): a mechanical model for the related microseismicity. Tectonophysics 359, 97–115.

Collettini, C., Holdsworth, R.E., 2004. Fault zone weakening and character of slip along low-angle normal faults: insights from the Zuccale fault, Isle of Elba, Italy. Journal of the Geological Society of London 161, 1039–1051.

Deer, W.A., Howie, R.A., Zussman, J., 1962. An Introduction to the Rock Forming Minerals: Micas. Longman Group Limited, London.

Di Toro, G., Hirose, T., Nielsen, S., Pennacchioni, G., Shimamoto, T., 2006. Natural and experimental evidence of melt lubrication of faults during earthquakes. Science 311, 647–649.

Dieterich, J.H., 1978. Time-dependent friction and the mechanics of stick-slip. Pure and Applied Geophysics (Historical Archive) 116, 790–806.

Evans, J.P., Chester, F.M., 1995. Fluid-rock interaction in faults of the San Andreas system: inferences from San Gabriel fault rock geochemistry and microstructures. Journal of Geophysical Research 100, 13007–13020.

Faulkner, D.R., Rutter, E.H., 2001. Can the maintenance of overpressured fluids in large strike-slip fault zones explain their apparent weakness? Geology 29, 503–506.

Gleason, G.C., Tullis, J., 1995. A flow law for dislocation creep of quartz aggregates determined with the molten salt cell. Tectonophysics 247, 1–23.

Goetze, C., Evans, B., 1979. Stress and temperature in the bending lithosphere as constrained by experimental rock mechanics. Geophysical Journal International 59, 463–478.

He, C., Wang, Z., Yao, W., 2007. Frictional sliding of gabbro gouge under hydrothermal conditions. Tectonophysics 445, 353–362.

He, C., Yao, W., Wang, Z., Zhou, Y., 2006. Strength and stability of frictional sliding of gabbro gouge at elevated temperatures. Tectonophysics 427, 217–229.

Hickman, S.H., 1991. Stress in the lithosphere and the strength of active faults. Review of Geophysics 29, 759–775.

Hickman, S.H., Sibson, R.H., Bruhn, R., 1995. Introduction to special section: mechanical involvement of fluids in faulting. Journal of Geophysical Research 100, 12831–12840.

Holdsworth, R.E., 2004. Weak faults – rotten cores. Science 303, 181–182.

Holdsworth, R.E., Stewart, M., Imber, J., Strachan, R.A., 2001. The structure and rheological evolution of reactivated continental fault zones: a review and case study. In: Miller, J.A., Holdsworth, R.E., Buick, I.S., Handy, M.R. (Eds.), Continental Reactivation and Reworking, vol. 184. Geological Society of London, pp. 115–137.

Huang, W.L., Wyllie, P.J., 1974. Melting relations of muscovite with quartz and sanidine in the K2O-Al2O3-SiO2-H2O system to 30 kilobars and an outline of paragonite melting relations. American Journal of Science 274, 378–395.

Ikari, M.J., Saffer, D.M., Marone, C., 2007. Effect of hydration state on the frictional properties of montmorillonite-based fault gouge. Journal of Geophysical Research 112. doi:10.1029/2006JB004748.

Imber, J., Holdsworth, R.E., Butler, C.A., Lloyd, G.E., 1997. Fault-zone weakening processes along the reactivated Outer Hebrides Fault Zone, Scotland. Journal of the Geological Society of London 154, 105–109.

Jefferies, S.P., Holdsworth, R.E., Shimamoto, T., Takagi, H., Lloyd, G.E., Spiers, C.J., 2006a. Origin and mechanical significance of foliated cataclastic rocks in the cores of crustal-scale faults: examples from the Median Tectonic Line, Japan. Journal of Geophysical Research 111. doi:10.1029/2005JB004205.

Jefferies, S.P., Holdsworth, R.E., Wibberley, C.A.J., Shimamoto, T., Spiers, C.J., Niemeijer, A.R., Lloyd, G.E., 2006b. The nature and importance of phyllonite development in crustal-scale fault cores: an example from the Median Tectonic Line, Japan. Journal of Structural Geology 28, 220–235.

Kanagawa, K., 2002. Frictional behavior of synthetic gouge-bearing faults under the operation of pressure solution. Earth Planets and Space 54, 1147–1152.

Kanagawa, K., Cox, S.F., Zhang, S., 2000. Effects of dissolution–precipitation processes on the strength and mechanical behavior of quartz gouge at high-temperature hydrothermal conditions. Journal of Geophysical Research 105, 11,115–11,126.

Kronenberg, A.K., Kirby, S.H., Pinkston, J., 1990. Basal slip and mechanical anisotropy of biotite. Journal of Geophysical Research 95, 19257–19278.

Lachenbruch, A.H., Sass, J.H., 1980. Heat flow and energetic of the San Andreas fault zone. Journal of Geophysical Research 85, 6185–6223.

Lehner, F.K., Bataille, J., 1984. Nonequilibrium thermodynamics of pressure solution. Pure and Applied Geophysics 122, 53–85.

Logan, J.M., Rauenzahn, K.A., 1987. Frictional dependence of gouge mixtures of quartz and montmorillonite on velocity, composition and fabric. Tectonophysics 144, 87–108.

Mares, V.M., Kronenberg, A.K., 1993. Experimental deformation of muscovite. Journal of Structural Geology 15, 1061–1075.

Mariani, E., Brodie, K.H., Rutter, E.H., 2006. Experimental deformation of muscovite shear zones at high temperatures under hydrothermal conditions and the strength of phyllosilicate-bearing faults in nature. Journal of Structural Geology 28, 1569–1587.

Meike, A., 1989. In situ-deformation of micas: a high-voltage electron-microscope study. American Mineralogist 74, 780–796.

Miller, S.A., Nur, A., Olgaard, D.L., 1996. Earthquakes as a coupled shear stress-high pore pressure dynamical system. Geophysical Research Letters 23, 197–200.

Miller, S.A., Olgaard, D.L., 1997. Modeling seismicity clustering and fault weakness due to high pore pressures. Physics and Chemistry of The Earth 22, 43–48.

Moore, D.E., Lockner, D.A., 2004. Crystallographic controls on the frictional behavior of dry and water-saturated sheet structure minerals. Journal of Geophysical Research 109. doi:10.1029/2003JB002582.

Moore, D.E., Lockner, D.A., 2007. Comparative deformation behavior of minerals in serpentinite ultramafic rock: application to the slab–mantle interface in subduction zones. International Geology Review 49, 401–415.

Moore, D.E., Lockner, D.A., Shengli, M., Summers, R., Byerlee, J.D., 1997. Strengths of serpentinite gouges at elevated temperatures. Journal of Geophysical Research 102, 14787–14801.

Moore, D.E., Rymer, M.J., 2007. Talc-bearing serpentinite and the creeping section of the San Andreas fault. Nature 448, 795–797.

Morrow, C.A., Moore, D.E., Lockner, D.A., 2000. The effect of mineral bond strength and adsorbed water on fault gouge frictional strength. Geophysical Research Letters 27, 815–818.

Morrow, C.A., Radney, B., Byerlee, J.D., 1992. Frictional strength and the effective pressure law of montmorillonite and illite clays. In: Evans, B., Wong, T.-F. (Eds.), Fault Mechanics and Transport Properties of Rocks. Academic, San Diego, CA, pp. 69–88.

Nakatani, M., Scholz, C.H., 2004. Frictional healing of quartz gouge under hydro-thermal conditions: 1. Experimental evidence for solution transfer healing mechanism. Journal of Geophysical Research 109. doi:10.1029/2001JB001522.

Niemeijer, A.R., Spiers, C.J., 2005. Influence of phyllosilicates on fault strength in the brittle-ductile transition: insights from rock analogue experiments. In: Bruhn, D., Burlini, L. (Eds.), High Strain Zones: Structure and Physical Properties, vol. 245. Geological Society of London, pp. 303–327.

Niemeijer, A.R., Spiers, C.J., 2006. Velocity dependence of strength and healing behaviour in simulated phyllosilicate-bearing fault gouge. Tectonophysics 427, 231–253.

Niemeijer, A.R., Spiers, C.J., 2007. A microphysical model for strong velocity weakening in phyllosilicate-bearing fault gouges. Journal of Geophysical Research 112. doi:10.1029/2007JB005008.

Niemeijer, A.R., Spiers, C.J., Bos, B., 2002. Compaction creep of quartz sand at 400–600 C: experimental evidence for dissolution-controlled pressure solution. Earth and Planetary Science Letters 195, 261–275.

Niemeijer, A.R., Spiers, C.J., Peach, C.J., 2008. Frictional behaviour of simulated quartz fault gouges under hydrothermal conditions: results from ultra-high strain rotary shear experiments. Tectonophysics 460, 288–303.

O'Hara, K., 2007. Reaction weakening and emplacement of crystalline thrusts: diffusion control on reaction rate and strain rate. Journal of Structural Geology 29, 1301–1314.

Ranalli, G., 1995. Rheology of the Earth. Chapman & Hall. 413p.

Rawling, G.C., Goodwin, L.B., 2003. Cataclasis and particulate flow in faulted, poorly lithified sediments. Journal of Structural Geology 25, 317–331.

Rutter, E.H., Holdsworth, R.E., Knipe, R.J., 2001. The nature and tectonic significance of fault zone weakening: an introduction. In: Holdsworth, R.E., Strachan, R.A., Magloughlin, J.F., Knipe, R.J. (Eds.), The Nature and Tectonic Significance of Fault Zone Weakening, vol. 186. Geological Society of London, pp. 1–11.

Rutter, E.H., Maddock, R.H., 1992. On the mechanical properties of synthetic kao-lintie/quartz fault gouge. Terra Nova 4, 489–500.

Rutter, E.H., Maddock, R.H., Hall, S.H., White, S.H., 1986. Comparative microstructures of natural and experimentally produced clay-bearing fault gouges. Pure and Applied Geophysics (Historical Archive) 124, 3–30.

SAFOD core atlas, v.., 2007. Available from: www.earthscope.org.

Saileswaran, N., Panchanathan, V., 1973. Compaction of grains. General parameter evaluation. Powder Technology 8, 19–26.

Sammis, C.G., King, G., Biegel, R.L., 1987. The kinematics of gouge deformation. Pure and Applied Geophysics 125, 777–812.

Schleicher, A.M., Tourscher, S.N., van der Pluijm, B.A., Warr, L.N., 2009a. Constraints on mineralization, fluid-rock interaction, and mass transfer during faulting at 2–3 km depth from the SAFOD drill hole. Journal of Geophysical Research 114.

Schleicher, A.M., van der Pluijm, B.A., Warr, L.N., 2008. What Controls Creep on the San Andreas Fault at the SAFOD Drillhole? Eos Transactions AGU 89 (53) Fall Meet. Suppl. Abstract T13A–1910.

Schleicher, A.M., Warr, L.N., van der Pluijm, B.A., 2009b. On the origin of mixed-layered clay minerals from the San Andreas Fault at 2.5–3 km vertical depth (SAFOD drillhole at Parkfield, California). Contributions to Mineralogy and Petrology 157, 173–187.

Scholz, C.H., 2002. The Mechanics of Earthquakes and Faulting, second ed. Cambridge University Press Cambridge, UK. 471pp.

Scruggs, V.J., Tullis, T.E., 1998. Correlation between velocity dependence of friction and strain localization in large displacement experiments on feldspar, muscovite and biotite gouge. Tectonophysics 295, 15–40.

Shea, W.T., Kronenberg, A.K., 1992. Rheology and deformation mechanisms of an isotropic mica schist. Journal of Geophysical Research 97, 15201–15237.

Shimamoto, T., Logan, J.M., 1981. Effects of simulated clay gouges on the sliding behavior of Tennessee sandstone. Tectonophysics 75, 243–255.

Sibson, R.H., 1983. Continental fault structure and the shallow earthquake source. Journal of the Geological Society of London 140, 741–767.

Sibson, R.H., 2004. Controls on maximum fluid overpressure defining conditions for mesozonal mineralisation. Journal of Structural Geology 26, 1127–1136.

Sleep, N.H., 1995. Ductile creep, compaction, and rate and state dependent friction within major fault zones. Journal of Geophysical Research 100, 13065–13080.

Takahashi, M., Mizoguchi, K., Kitamura, K., Masuda, K., 2007. Effects of clay content on the frictional strength and fluid transport property of faults. Journal of Geophysical Research 112. doi:10.1029/2006JB004678.

Tembe, S., Lockner, D.A., Solum, J.G., Morrow, C.A., Wong, T.-F., Moore, D.E., 2006a. Frictional strength of cuttings and core from SAFOD drillhole phases 1 and 2. Geophyscial Research Letters 33. doi:10.1029/2006GL027626.

Tembe, S., Lockner, D.A., Wong, T.-F., 2006b. Strength of SAFOD fault gouge under hydrothermal conditions. Eos Transactions AGU 87 Abstract S23C-0181.

Theiler, G., Gradt, T., 2008. Influence of the temperature on the tribological behaviour of PEEK composites in vacuum environment. Journal of Physics: Conference Series 100. doi:10.1088/1742-6596/100/7/072040.

Townend, J., Zoback, M.D., 2004. Regional tectonic stress near the San Andreas fault in central and southern California. Geophysical Research Letters 31. doi:10.1029/2003GL018918.

White, S.H., Bretan, P.G., Rutter, E.H., 1986. Fault-zone reactivation: kinematics and mechanisms. Philosophical Transactions of the Royal Society of London A317, 81–97.

Wibberley, C.A.J., 1999. Are feldspar-to-mica reactions necessarily reaction-softening processes in fault zones? Journal of Structural Geology 21, 1219–1227.

Wintsch, R.P., Christoffersen, R., Kronenberg, A.K., 1995. Fluid-rock reaction weakening of fault zones. Journal of Geophysical Research 100, 13021–13032.

Wu, F.T., Blatter, L., Roberson, H., 1975. Clay gouges in the San Andreas Fault System and their possible implications. Pure and Applied Geophysics (Historical Archive) 113, 87–95.

Zhang, S., Tullis, T.E., Scruggs, V.J., 2001. Implications of permeability and its anisotropy in a mica gouge for pore pressures in fault zones. Tectonophysics 335, 37–50.

Zoback, M.D., Hickman, S.H., Ellsworth, W., Kirschner, D., Pennell, N.B., Chery, J., Sobolev, S., 2007. Preliminary Results from SAFOD Phase 3: implications for the state of stress and shear localization in and near the San Andreas Fault at depth in central California. Eos Transactions AGU 88 (52) Fall Meet. Suppl. Abstract T13 G-03.

Zoback, M.D., Zoback, M.L., Mount, V.S., Suppe, J., Eaton, J.P., Healy, J.H., Oppenheimer, D., Reasenberg, P., Jones, L., Rayleigh, C.B., Wong, I.G., Scotti, O., Wentworth, C., 1987. New evidence on the state of stress of the San Andreas fault system. Science 238, 1105–1111.